Combining Discrete Equations Method and Upwind Downwind-Controlled Splitting for non-reacting and reacting two-fluid computations: Two dimensional case

Kunkun Tang[a,1,*], Alberto Beccantini[a], Christophe Corre[b]

a Atomic Energy and Alternative Energies Commission - CEA Saclay,
Laboratory of Thermal Hydraulics and Fluid Mechanics,
DEN/DM2S/STMF/LATF, 91191 Gif-sur-Yvette, France
b Grenoble-INP/UJF Grenoble/CNRS LEGI UMR5519, Grenoble, France

Abstract

This work deals with impermeable and permeable interfaces and the design of numerical strategies allowing multi-dimensional propagation of these interfaces on general unstructured grids. The numerical context is the (Reactive) Discrete Equations Method (DEM/RDEM) for the Baer-Nunziato type non-equilibrium multiphase model allowing a diffused interface, and meanwhile preserving the global conservation, which is of fundamental importance for studying long term combustion phenomena in large-scale geometries. Another advantage of RDEM for combustion lies in its ability to compute both deflagration and detonation, provided an appropriate reactive Riemann solver is inserted within the method. The present paper is a sequel to the recent publication (Tang et *al.*, 2014) where an anti-diffusive approach and an original Upwind Downwind-Controlled Splitting method (UDCS) were combined with the 1D formulation of the DEM and RDEM. The method successfully developed in 1D for computing inert interfaces (e.g. impermeable water gas shock tube problem) and flame interfaces (e.g. Chapman-Jouguet deflagration and strong detonation wave) with excellent robustness and accuracy properties is extended here to two dimensional problems. The proposed low- and anti-diffusive versions of the multi-D UDCS strategy form an original contribution to the modeling of multifluid flows on unstructured grids. This multi-D extension relies on a general derivation of the *Downwind Factors* involved in the formulation of UDCS. In particular, the proposed UDCS anti-diffusive algorithm represents a new alternative to the "Extended–Vofire" solver (Faucher and Kokh, 2013) for unstructured meshes. Numerical experiments performed for non-reacting gas-gas and liquid-gas shock bubble interactions as well as for a model combustion problem demonstrate the combination of DEM/RDEM with UDCS yields excellent robustness/accuracy properties. Some remaining issues linked to the modeling of flame propagation in multi-dimensional cases are eventually discussed.

Keywords:
compressible multifluid flows, reactive interface, two-fluid model, Baer-Nunziato model, non-conservative system, (Reactive) Discrete Equations Method, Diffuse Interface approach, anti-diffusive scheme on unstructured meshes, Upwind Downwind-Controlled Splitting, reactive Riemann problem, multi-dimensional unstructured grid, air-R22 shock bubble interaction, liquid-gas shock bubble interaction, combustion and flame propagation

*Corresponding author. Tel.: +33 1 69 08 97 24.
Email addresses: kunkun.tang@inria.fr (Kunkun Tang), alberto.beccantini@cea.fr (Alberto Beccantini)
[1] Present address: Inria Bordeaux Sud-Ouest, Team Bacchus, 200 avenue de la Vieille Tour, 33405 Talence, France

1. Introduction

The Discrete Equations Method (DEM) was proposed by Abgrall and Saurel, 2003 [1] with the aim of computing compressible multiphase flows. When interface problems are involved, DEM belongs to

the family of *Diffuse Interface* approaches. Chinnayya et *al.*, 2004 [7] first extended the original DEM to the reactive case of detonation waves using operator splitting for reaction source terms on 2D structured meshes. Le Métayer et *al.*, 2005 [25] then extended DEM to RDEM for the modeling of evaporation and detonation fronts using a reactive Riemann solver, where the Chapman-Jouguet (CJ) deflagration and CJ detonation points are respectively imposed. Next, Beccantini and Studer, 2010 [4] proposed a reactive Riemann solver in which the transition from deflagration to detonation is continuous with respect to the *fundamental flame speed*, and they first succeeded to compute both deflagration and detonation flows using the RDEM approach on unstructured meshes. Two major numerical difficulties were however identified:

a) The first-order RDEM method is robust, but yields a very diffusive flame profile for fast deflagration and detonation waves, which spoils the global accuracy of flow quantities in the flame region;

b) The quasi second-order RDEM method with a limiting approach and Predictor-Corrector time stepping improves the accuracy, especially for the flame front. However, robustness limitations appear in the multi-dimensional case so that very small Courant numbers are sometimes required.

With the objective to solve the aforementioned issues, the present 2D paper together with our previous 1D work [35] addresses high order DEM/RDEM approach and proposes an original numerical algorithm for both inert and reactive (deflagration and detonation) interface problems. Note the problem of properly extending the DEM/RDEM approach to the multi-dimensional case has also been recently addressed by Franquet and Perrier in the framework of the Discontinuous Galerkin approach [17, 16, 18]. The key ingredient of the novel numerical strategy proposed in the present contribution consists in combining DEM/RDEM with an Upwind Downwind-Controlled Splitting (UDCS) strategy. The proposed second-order low-diffusive and anti-diffusive versions of this multi-D UDCS approach represent an original contribution to the modeling of multifluid flows on unstructured meshes.

As previously mentioned in [34, 35], the basic idea behind the coupling between DEM/RDEM and

UDCS is to improve to second-order the accuracy of the first-order version of DEM/RDEM while preserving a robustness level similar to the one offered by the first-order method. This scheme relies indeed upon the idea of redistributing volume, mass, momentum and energy at the numerically diffused interface region, while satisfying global conservation conditions (mass, momentum, and energy leaving one phase enter into the other phase). The essential strategy of the proposed approach involves two steps: an "upwind step" where the first-order upwind method is employed in the DEM/RDEM approach, and a "downwind-controlled step" where part of the numerically diffused volume is moved back to its upwind cell element while fulfilling the Local Extremum Diminishing (LED) property (see [21] for details on LED). This second step can be expressed using classical second-order limiters available in the literature or an anti-diffusive approach (see [35]). As will be demonstrated in the present contribution, the extension of the approach to multi-dimensional unstructured meshes is straightforward when a second-order limiting strategy is retained. The anti-diffusive UDCS approach can also be readily extended to multi-dimensional problem in each grid element, provided the quantity to be distributed for "downwinding" on outlet intercell boundaries, in the second step of UDCS, is assumed proportional to the quantity previously "upwinded" in the first step.

The proposed multi-dimensional UDCS anti-diffusive approach represents an alternative to the "Vofire" method [10, 15]. Indeed, in "Vofire", anti-diffusion is obtained by decomposing intercell boundaries in order to yield, in each element, several pseudo-1D problems involving only one inlet and one outlet intercell boundary. In the presently proposed approach, all the inlet intercell boundaries are merged together on one hand as well as the outlet boundaries on the other hand, in order to yield a single pseudo 1D problem to deal with.

As will be demonstrated, the resulting multi-D UDCS scheme yields the following two main advantages:

a) Both the second-order and the anti-diffusive UDCS schemes combined with DEM/RDEM are as robust as a first-order scheme.

b) The developed second-order or anti-diffusive UDCS method considerably improves the accuracy of the first-order DEM/RDEM method for both impermeable and permeable interfaces on unstructured meshes.

Note that the reactive Riemann solver [4] inserted into RDEM in this work has the capability of computing a wide range of combustion regimes without resorting to operator splitting: weak deflagration, Chapman-Jouguet deflagration, Chapman-Jouguet detonation, strong detonation and deflagration to detonation transition can all be addressed. The ability of the UDCS anti-diffusive method coupled with RDEM to compute a quasi exact 1D reactive shock has been established in [35]. The present work demonstrates it can also sharply resolve a 2D reactive shock. The present paper is focused on the numerical solution of the two-phase flow model so that the reader is referred to [4] for more details on the reactive Riemann solver used in this work for dealing with the reaction mass transfer terms appearing at the interface.

The article is organized as follows: Section 2 is devoted to two dimensional DEM/RDEM, and mainly to the derivation of the 2D UDCS scheme for the scalar topological (transport) equation appearing in DEM/RDEM for the Baer-Nunziato type two-phase flow model [11, 33, 35]. In particular, downwind factors for both second-order and anti-diffusive versions of UDCS are presented. For the sake of conciseness, the present paper is supposed to be read as a follow-up of [35] where a detailed description of the physical model, the equations of state (EOS) and the (Reactive) Discrete Equations Method is available and thus not reproduced here. The proposed method is next assessed in Section 3 on three carefully selected test problems. Conclusions follow, which summarize the main benefits obtained from using the multi-dimensional UDCS approach within the DEM/RDEM framework and provide a few references to recent publications making use of the developed second-order RDEM approach for performing combustion simulations in large-scale geometries. Details on the numerical discretization of the non-conservative flux term and the numerical fluxes involved in the multi-dimensional DEM/RDEM approach are reported in Appendix A while the multi-dimensional limiter used for the quasi second-order variable reconstruction is thoroughly described in Appendix B.

2. Multi-D Discrete Equations Method and Upwind Downwind-Controlled Splitting: an original algorithm of low- and anti-diffusive scheme on unstructured grids

Building upon the previous 1D contribution [35], the objective of the present work is to solve the following two-fluid system (the phase index $k \in \{1, 2\}$) for interfaces that might involve chemical reactions:

$$\frac{\partial (\alpha_k \mathbf{U}_k)}{\partial t} + \nabla \cdot (\alpha_k \mathbf{F}_k) = (\mathbf{F}_{k,I} - \mathbf{U}_{k,I} \mathbf{D}_I) \cdot \nabla \alpha_k, \quad (1)$$

with

$$\mathbf{U} = \begin{bmatrix} 1 \\ \rho \\ \rho \mathbf{v} \\ \rho \tilde{e}_t \end{bmatrix}, \mathbf{F} = \begin{bmatrix} 0 \\ \rho \mathbf{v} \\ \rho \mathbf{v} \mathbf{v} + p \mathbf{I} \\ \rho \tilde{e}_t \mathbf{v} + p \mathbf{v} \end{bmatrix}.$$

The variable α is the volume fraction (*i.e.* the reaction progress variable [4] in a combustion case), ρ the density, $\mathbf{v}$ the flow velocity vector, p the pressure, $\tilde{e}_t$ the total energy. As explained in [4, 35], the thermal diffusivity and the species diffusion for combustion simulation are not taken into account; chemical reaction can only occur at the interface. The first equation in (1) corresponds to the topological (transport) equation

$$\frac{\partial \alpha_k}{\partial t} + \mathbf{D}_I \cdot \nabla \alpha_k = 0. \quad (2)$$

where $\mathbf{D}_I$ denotes the physical interface velocity (*i.e.* total flame velocity in case of combustion). Note that only the component

$$\mathbf{D}_I \cdot \mathbf{n}_k \quad (3)$$

needs to be defined, which corresponds to the velocity component perpendicular to the physical interface. Here $\mathbf{n}_k$ is the normal unit vector pointing toward the outside of phase Σ_k.

The two-phase model (1) can be reformulated as follows:

$$\frac{\partial (\alpha_k \mathbf{U}_k)}{\partial t} + \nabla \cdot (\alpha_k \mathbf{F}_k) = \mathbf{M}_{k,I} \cdot \nabla \alpha_k + \mathbf{G}_{k,I} \cdot \nabla \alpha_k, \quad (4)$$

3

with

$$\mathbf{M} \;=\; \mathbf{U}(\mathbf{v}-\mathbf{D}) \;=\; \begin{bmatrix} (\mathbf{v}-\mathbf{D}) \\ \rho(\mathbf{v}-\mathbf{D}) \\ \rho\mathbf{v}(\mathbf{v}-\mathbf{D}) \\ \rho\tilde{e}_t(\mathbf{v}-\mathbf{D}) \end{bmatrix},$$

$$\mathbf{G} \;=\; \mathbf{F}-\mathbf{U}\mathbf{v} \;=\; \begin{bmatrix} -\mathbf{v} \\ 0 \\ p\mathbf{I} \\ p\mathbf{v} \end{bmatrix}.$$

Here $\mathbf{M}_{k,I}$ represents the mass transfer at the interface. For non-reacting problems (for instance the shock bubble interaction test-cases computed in this work) $\mathbf{M}_{k,I}$ vanishes. Note the two-fluid system (1) or (4) is often referred to as a Baer-Nunziato type model [2] in the literature (see for instance [36, 39]).

One of the key objectives of the present work is to obtain a numerical model capable of simulating high speed (both subsonic and supersonic) combustion waves, in which case the mass transfer rate across the flame interface is significant, and the chemical evolution is assumed to be governed by one irreversible, infinitely fast chemical reaction. For this reason, no assumption of mechanical or chemical equilibrium [39] in the two-phase model (1) or (4) is made in this work. Note indeed that the assumption of mechanical equilibrium is valid if the mass transfer rate is zero or negligible (see [20, pp. 38–43]), for instance when chemical equilibrium is reached, or when very slow deflagrations take place. When dealing with the non-reacting interface problems considered in this paper, where no mass transfer occurs, the addition of relaxation terms [29, 39] to the model (1) or (4) aiming to reach mechanical equilibrium does not have any visible impact on the computed numerical solutions [35], since, for interface problems separating pure fluids, no physical mixture is present. Thus, the non-equilibrium model (1) is used in this work for both non-reacting and reacting interfaces.

As a first support for discussing the numerical aspects involved in the solution of the above two-fluid system, a typical element $\mathcal{C}_i$ of a two-dimensional unstructured grid is displayed in Fig. 1. Its boundaries $\{\partial\mathcal{C}_{i,j}\}$ can be divided into two categories: *inlet* (denoted as $\{\partial\mathcal{C}_{i,\mathrm{in},j}\}$) and *outlet* (denoted as $\{\partial\mathcal{C}_{i,\mathrm{out},j}\}$) ones. An inlet boundary $\partial\mathcal{C}_{i,\mathrm{in},j}$ for

phase Σ_k is characterized by

$$\mathbf{D}^n_{i,\mathrm{in},j}\cdot\mathbf{n}_{i,\mathrm{in},j}<0, \tag{5}$$

with $\mathbf{n}_{i,\mathrm{in},j}$ the normal unit vector pointing toward the outside of $\mathcal{C}_i$. That is, the numerical interface enters inside $\mathcal{C}_i$, which generates a (positive or negative) volume of Σ_k. Here $\mathbf{D}^n_{i,\mathrm{in},j}$ has been assumed to be the inlet numerical interface velocity. On the other hand, an outlet boundary $\partial\mathcal{C}_{i,\mathrm{out},j}$ is such that

$$\mathbf{D}^n_{i,\mathrm{out},j}\cdot\mathbf{n}_{i,\mathrm{out},j}>0, \tag{6}$$

with $\mathbf{n}_{i,\mathrm{out},j}$ pointing also toward the outside. $\mathbf{D}^n_{i,\mathrm{out},j}$ is the outlet numerical interface velocity.

When solving system (1) using (Reactive) Discrete Equations Method (DEM/RDEM) [1, 25], as explained in our previous work [35, Section 3], an important procedure consists in the *intercell surface partition*. In the 2D case, considering for instance an intercell boundary $\partial\mathcal{C}_{i,\mathrm{in},j}$ in Fig. 1, the solutions of two or three local Riemann problems for (reactive) Euler equations are required among four possibilities (see the right part of Fig. 1, where $\vec{z}$ is perpendicular to the 2D domain). Indeed, at least both of the two single-phase Riemann problems (for Euler equations) should always be solved. Furthermore, if $\alpha^n_{i,\mathrm{in},j} - \alpha^n_i \neq 0$, one additional two-phase (inert or reactive) Riemann problem (for Euler equations) needs to be solved. Here $\alpha^n_{i,\mathrm{in},j}$ and α^n_i are the volume fractions of cell $\mathcal{C}_{i,\mathrm{in},j}$ and $\mathcal{C}_i$, respectively (see also Fig. 2). The obtained numerical fluxes related to their corresponding *partial surface area* are then used to update the space average of conserved variables. Appendix A details how to deal with the non-conservative flux term involved in (1), and also summarize both the conservative and non-conservative numerical fluxes required in DEM/RDEM to update the space averages.

It should be underlined that, in multi-D DEM/RDEM, the numerical interface velocities in (5) and (6) are provided by the local 1D two-phase (reactive) Riemann problem solution, which aims at approximating (3) and thus at updating the volume fraction.

In the case of reactive interface with mass transfer, the conservative flux $\mathbf{F}_k$, together with interfacial fluxes $\mathbf{M}_{k,I}$ and $\mathbf{G}_{k,I}$ in (4) are solved all at once ($\mathbf{M}_{k,I} + \mathbf{G}_{k,I}$ corresponds to the *Lagrangian Flux*,
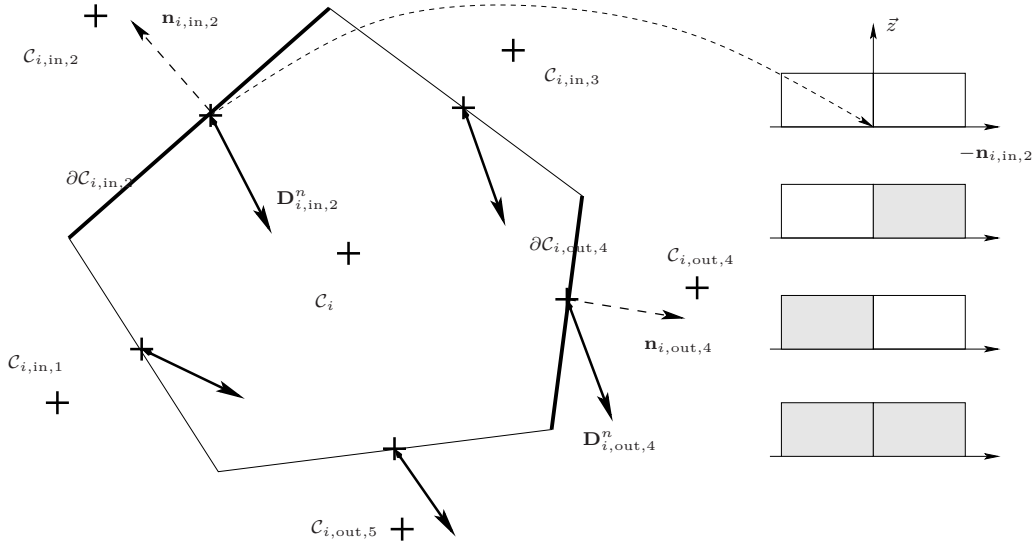
4

Figure 1: A typical two dimensional Finite Volume element. Illustration of (Reactive) Discrete Equations Method (DEM/RDEM). At each intercell boundary, resolutions of two or three local Riemann problems for (reactive) Euler equations are required among four possibilities. $\vec{z}$ is perpendicular to the 2D domain. The obtained numerical interface velocities and fluxes related to their corresponding partial surface area are then used to update the volume fraction and space average of conserved variables, respectively [35]. Grey represents phase Σ_1, and white is phase Σ_2.

as explained in Appendix A) inside the 1D local reactive Riemann solver for Euler equations without performing operator splitting (similar to [25]), which differs from some works in the literature for the solution of Baer-Nunziato type model, for instance [39] where the mass transfer $\mathbf{M}_{k,I} \cdot \nabla \alpha_k$ is modeled by Gibbs free energy relaxation terms. Let us emphasize the Rankine–Hugoniot jump relations applied in the 1D reactive Riemann solver across the reactive shock (see also Appendix A) guarantee the interface conservation conditions in the normal direction of cell boundaries (where the reactive Riemann problem is solved).

As previously pointed out in [34, 35, 33], the DEM/RDEM algorithm is essentially focused on the topological transport equation (2). In fact, once (2) is properly solved, it only remains to update the conserved variables in each *partition volume region* using the solution of local Riemann problems (see [35, Section 3.1] and Appendix A).

Thus, let us now mainly focus on the scalar topological equation (2) and on how to derive the multi-D UDCS scheme, a 1D version of which was previously proposed in [35] in the framework of DEM/RDEM. For the sake of simplicity, a two dimensional case only is presented here but note

the ideas that are developed also hold for 3D problems. The phase index k is omitted from now on in this section since the UDCS scheme is the same for both phases.

The multi-D version of the first-order upwind DEM/RDEM scheme [1, 35] on unstructured meshes for the topological equation (2) can be summarized as follows

$$\alpha_i^{n+1,\mathrm{up}} = \alpha_i^n + \sum_{j \in \{\mathrm{in}\}} \frac{\Delta \mathrm{up}_{i,\mathrm{in},j}^n}{|\mathcal{C}_i|}, \qquad (7)$$

with $|\mathcal{C}_i|$ the volume of $\mathcal{C}_i$ and $\Delta \mathrm{up}_{i,\mathrm{in},j}^n$ the volume of Σ_k entering into $\mathcal{C}_i$ through the inlet boundary $\partial \mathcal{C}_{i,\mathrm{in},j}$ and defined by

$$\Delta \mathrm{up}_{i,\mathrm{in},j}^n = \\ \left(\alpha_{i,\mathrm{in},j}^n - \alpha_i^n\right) |\partial \mathcal{C}_{i,\mathrm{in},j}| \left|\mathbf{D}_{i,\mathrm{in},j}^n \cdot \mathbf{n}_{i,\mathrm{in},j}\right| \Delta t, \qquad (8)$$

with $|\partial \mathcal{C}_{i,\mathrm{in},j}|$ the interfacial surface area of $\partial \mathcal{C}_{i,\mathrm{in},j}$.

Scheme (7) is graphically described in Fig. 2 and Fig. 3. An inlet cell boundary $\partial \mathcal{C}_{i,\mathrm{in},j}$ (see Fig. 1) is considered in Fig. 2. The volume $\Delta \mathrm{up}_{i,\mathrm{in},j}^n$ contributes to the updating of volume fraction in cell $\mathcal{C}_i$. A detailed derivation of $\Delta \mathrm{up}_{i,\mathrm{in},j}^n$ from the discretization of non-conservative flux term in (1)
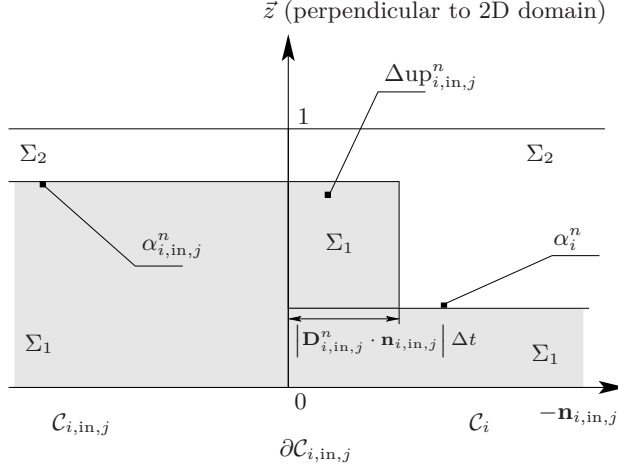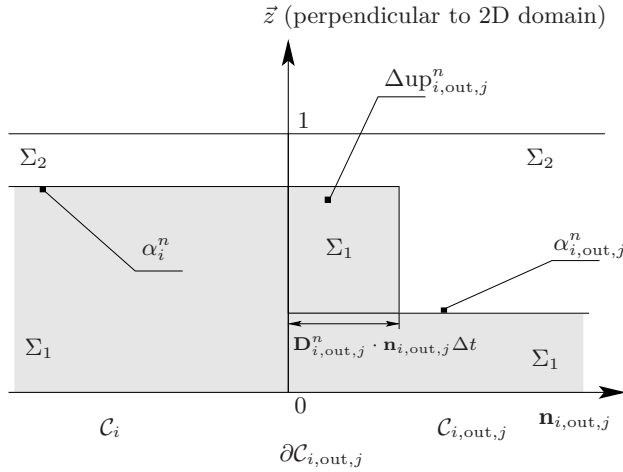
Figure 2: Multi-D (Reactive) Discrete Equations Method (DEM/RDEM) on unstructured grids. The $\vec{z}$ direction along which α is measured is perpendicular to the considered 2D domain. Phase Σ_1 and Σ_2 are respectively displayed in grey and white. Two single-phase and one two-phase (reactive) local Riemann problems for Euler equations require to be resolved. The numerical interface enters inside $\mathcal{C}_i$, which generates a positive volume $\Delta \mathrm{up}^n_{i,\mathrm{in},j}$ of Σ_1.

Figure 3: Multi-D (Reactive) Discrete Equations Method (DEM/RDEM) on unstructured grids. The $\vec{z}$ direction along which α is measured is perpendicular to the considered 2D domain. Phase Σ_1 and Σ_2 are respectively displayed in grey and white. Two single-phase and one two-phase (reactive) local Riemann problems for Euler equations require to be resolved. The numerical interface goes toward the outside of $\mathcal{C}_i$, which does not contribute to the volume fraction update for cell $\mathcal{C}_i$. Meanwhile, it generates a positive volume $\Delta \mathrm{up}^n_{i,\mathrm{out},j}$ of Σ_1 for the adjacent cell $\mathcal{C}_{i,\mathrm{out},j}$.

can be found in Appendix A.

On the other hand, when an outlet cell boundary $\partial \mathcal{C}_{i,\mathrm{out},j}$ is concerned as illustrated in Fig. 3, the generated volume

$$\Delta \mathrm{up}^n_{i,\mathrm{out},j} =$$

$$\left(\alpha^n_i - \alpha^n_{i,\mathrm{out},j}\right) |\partial \mathcal{C}_{i,\mathrm{out},j}| \, \mathbf{D}^n_{i,\mathrm{out},j} \cdot \mathbf{n}_{i,\mathrm{out},j} \Delta t. \tag{9}$$

does not contribute to the volume fraction updating for cell $\mathcal{C}_i$. However, this volume should be taken into account for updating α in the adjacent cell $\mathcal{C}_{i,\mathrm{out},j}$.

The upwind formulation (7) can be rearranged as follows:

$$\alpha^{n+1,\mathrm{up}}_i$$

$$= \alpha^n_i \left(1 - \frac{\Delta t}{|\mathcal{C}_i|} \sum_{j \in \{\mathrm{in}\}} |\partial \mathcal{C}_{i,\mathrm{in},j}| \left|\mathbf{D}^n_{i,\mathrm{in},j} \cdot \mathbf{n}_{i,\mathrm{in},j}\right|\right)$$

$$+ \sum_{j \in \{\mathrm{in}\}} \alpha^n_{i,\mathrm{in},j} \left(\frac{\Delta t}{|\mathcal{C}_i|} |\partial \mathcal{C}_{i,\mathrm{in},j}| \left|\mathbf{D}^n_{i,\mathrm{in},j} \cdot \mathbf{n}_{i,\mathrm{in},j}\right|\right). \tag{10}$$

Since the time step Δt is imposed in practice so as to satisfy:

$$\Delta t \leq \min_i \frac{|\mathcal{C}_i|}{\sum_{j \in \{\mathrm{in}\}} |\partial \mathcal{C}_{i,\mathrm{in},j}| \left|\mathbf{D}^n_{i,\mathrm{in},j} \cdot \mathbf{n}_{i,\mathrm{in},j}\right|}, \tag{11}$$

the quantity $\alpha^{n+1,\mathrm{up}}_i$ in (10) can thus be viewed as an average value between α^n_i and the set of values $\{\alpha^n_{i,\mathrm{in},j}\}$ for its inlet neighbors $\{\mathcal{C}_{i,\mathrm{in},j}\}$. This average value obviously satisfies the local Extremum Diminishing (LED) property [21]:

$$\alpha^{n+1}_i \in [m^n_i, M^n_i]. \tag{12}$$

where the local maximum and minimum values for $\mathcal{C}_i$ in (12) are computed as follows:

$$m^n_{i,\mathrm{in},j} = \min\{\alpha^n_i, \alpha^n_{i,\mathrm{in},j}\},$$
$$M^n_{i,\mathrm{in},j} = \max\{\alpha^n_i, \alpha^n_{i,\mathrm{in},j}\},$$
$$m^n_i = \min_j\{m^n_{i,\mathrm{in},j}\},$$
$$M^n_i = \max_j\{M^n_{i,\mathrm{in},j}\}. \tag{13}$$

It is worthwhile to notice that, when solving the scalar equation (2), the time step restriction (11) is a sufficient (but not necessary) condition to satisfy (12). Indeed, due to the inequality

$$\left|\sum_{j \in \{\mathrm{in}\}} \Delta \mathrm{up}^n_{i,\mathrm{in},j}\right| \leq \sum_{j \in \{\mathrm{in}\}} \left|\Delta \mathrm{up}^n_{i,\mathrm{in},j}\right|,$$

6

a larger Δt than the one given by (11) could still be able to ensure the LED condition (12).

Following the downwind factor idea introduced in [35, Section 5], and using the first-order Euler time discretization, the high resolution UDCS scheme designed for the multi-dimensional case reads:

$$\alpha_i^{n+1} = \alpha_i^n \quad + \sum_{j \in \{\text{in}\}} (1 - \lambda_{i,\text{in},j}^n) \frac{\Delta\text{up}_{i,\text{in},j}^n}{|\mathcal{C}_i|} \\ + \sum_{j \in \{\text{out}\}} \lambda_{i,\text{out},j}^n \frac{\Delta\text{up}_{i,\text{out},j}^n}{|\mathcal{C}_i|}, \quad (14)$$

or if including the "upwinded" state $\alpha_i^{n+1,\text{up}}$,

$$\alpha_i^{n+1} = \alpha_i^{n+1,\text{up}} \quad + \sum_{j \in \{\text{in}\}} (-\lambda_{i,\text{in},j}^n) \frac{\Delta\text{up}_{i,\text{in},j}^n}{|\mathcal{C}_i|} \\ + \sum_{j \in \{\text{out}\}} \lambda_{i,\text{out},j}^n \frac{\Delta\text{up}_{i,\text{out},j}^n}{|\mathcal{C}_i|}. \quad (15)$$

Note all downwind factors $\{\lambda\}$ have been assumed to be such that

$$0 \leq \lambda \leq 1.$$

Let us note that:

a) The scheme defined by (14) or (15) degenerates into the first-order upwind scheme when all the downwind factors vanish.

b) On the other hand, an unstable downwind scheme is recovered if setting all the downwind factors to unity.

Scheme (14) or (15) can be interpreted as follows: a part of the volume Δup_j^n generated and transported across the boundary $\partial\mathcal{C}_{i,j}$ by the first-order upwind method is moved back to its upwind cell (this part or volume percentage is precisely the downwind factor λ_j^n) . That is, based on the upwind result in $\mathcal{C}_i$, the quantity

$$\lambda_{i,\text{in},j}^n \Delta\text{up}_{i,\text{in},j}^n$$

is returned to the inlet neighbor $\mathcal{C}_{i,\text{in},j}$, and on the other hand the quantity

$$\lambda_{i,\text{out},j}^n \Delta\text{up}_{i,\text{out},j}^n$$

is retrieved from the outlet neighbor $\mathcal{C}_{i,\text{out},j}$. Large values of the downwind factors $\{\lambda_{i,\text{in},j}^n, \lambda_{i,\text{out},j}^n\}$,

make the scheme accurate but at the same time these downwind factors must be such that they allow the local LED condition (12) to remain satisfied.

2.1. UDCS second-order approach

As previously done in [35, Section 5] for a 1D problem, the UDCS second-order accurate scheme can be obtained by using a slope limiting strategy. In this framework, the value of the downwind factor $\lambda_{i,\text{out},j}^n$ for an outlet boundary is determined by

$$\lambda_{i,\text{out},j}^n = \frac{\alpha_i^n - \alpha_{\text{f},\text{out},j}^n}{\alpha_i^n - \alpha_{i,\text{out},j}^n}, \text{ when } \alpha_i^n \neq \alpha_{i,\text{out},j}^n. \quad (16)$$

The quantity $\alpha_{\text{f},\text{out},j}^n$ in (16) is the reconstructed value at the boundary $\partial\mathcal{C}_{i,\text{out},j}$ within cell $\mathcal{C}_i$ using a slope limiter. The value of the downwind factor $\lambda_{i,\text{in},j}^n$ for an inlet boundary is determined analogously:

$$\lambda_{i,\text{in},j}^n = \frac{\alpha_{i,\text{in},j}^n - \alpha_{\text{f},i,\text{in},j}^n}{\alpha_{i,\text{in},j}^n - \alpha_i^n}, \text{ when } \alpha_i^n \neq \alpha_{i,\text{in},j}^n. \quad (17)$$

Quantity $\alpha_{\text{f},i,\text{in},j}^n$ in (17) is the reconstructed value at the boundary $\partial\mathcal{C}_{i,\text{in},j}$ within cell $\mathcal{C}_{i,\text{in},j}$ using a slope limiter.

A modified version of the multi-dimensional Barth-Jespersen limiter is used in this work to obtain the reconstructed values $\alpha_{\text{f},\text{out},j}^n$ and $\alpha_{\text{f},i,\text{in},j}^n$ on volume fraction, and also those on primitive variables. Details on this multi-dimensional limiting strategy can be found in Appendix B.

2.2. UDCS anti-diffusive approach: an original algorithm of anti-diffusive scheme on unstructured grids

As an alternative to the previous strategy and for the sake of simplicity, a unique value of the downwind factor $\lambda_{i,\text{out}}^n$ defined for cell $\mathcal{C}_i$ can be imposed for all the outlet boundaries $\{\partial\mathcal{C}_{i,\text{out},j}\}$:

$$\lambda_{i,\text{out},j}^n = \lambda_{i,\text{out}}^n, \text{ for any } j.$$

Thus, by defining

$$\Delta\text{up}_{i,\text{out}}^n = \sum_{j \in \{\text{out}\}} \Delta\text{up}_{i,\text{out},j}^n$$

for cell $\mathcal{C}_i$, condition (12) is rewritten as the following inequalities:

$$\alpha_i^{n+1} = \alpha_i^n \quad + \sum_{j \in \{\text{in}\}} (1 - \lambda_{i,\text{in},j}^n) \frac{\Delta \text{up}_{i,\text{in},j}^n}{|\mathcal{C}_i|} \\ + \lambda_{i,\text{out}}^n \frac{\Delta \text{up}_{i,\text{out}}^n}{|\mathcal{C}_i|} \geq m_i^n, \tag{18}$$

$$\alpha_i^{n+1} = \alpha_i^n \quad + \sum_{j \in \{\text{in}\}} (1 - \lambda_{i,\text{in},j}^n) \frac{\Delta \text{up}_{i,\text{in},j}^n}{|\mathcal{C}_i|} \\ + \lambda_{i,\text{out}}^n \frac{\Delta \text{up}_{i,\text{out}}^n}{|\mathcal{C}_i|} \leq M_i^n. \tag{19}$$

It can be easily verified that, when setting $\lambda_{i,\text{out}}^n = 0$, both (18) and (19) are fulfilled for any value of $\lambda_{i,\text{in},j}^n$ by writing α_i^{n+1} as an average between α_i^n and the values of its inlet neighbors $\{\alpha_{i,\text{in},j}^n\}$ as similarly done in the formulation (10):

$$\alpha_i^{n+1} = \alpha_i^n \left(1 - \frac{\Delta t}{|\mathcal{C}_i|} \sum_{j \in \{\text{in}\}} \right. \\ (1 - \lambda_{i,\text{in},j}^n) |\partial \mathcal{C}_{i,\text{in},j}| \left| \mathbf{D}_{i,\text{in},j}^n \cdot \mathbf{n}_{i,\text{in},j} \right| \left. \right) + \sum_{j \in \{\text{in}\}} \\ \alpha_{i,\text{in},j}^n \left(\frac{\Delta t}{|\mathcal{C}_i|} (1 - \lambda_{i,\text{in},j}^n) |\partial \mathcal{C}_{i,\text{in},j}| \left| \mathbf{D}_{i,\text{in},j}^n \cdot \mathbf{n}_{i,\text{in},j} \right| \right). \tag{20}$$

Note (20) can be interpreted as an average, since the stability condition (11) allows to establish the following inequality :

$$\frac{\Delta t}{|\mathcal{C}_i|} (1 - \lambda_{i,\text{in},j}^n) |\partial \mathcal{C}_{i,\text{in},j}| \left| \mathbf{D}_{i,\text{in},j}^n \cdot \mathbf{n}_{i,\text{in},j} \right| \\ \leq \frac{\Delta t}{|\mathcal{C}_i|} \sum_{j \in \{\text{in}\}} (1 - \lambda_{i,\text{in},j}^n) |\partial \mathcal{C}_{i,\text{in},j}| \left| \mathbf{D}_{i,\text{in},j}^n \cdot \mathbf{n}_{i,\text{in},j} \right| \\ \leq \frac{\Delta t}{|\mathcal{C}_i|} \sum_{j \in \{\text{in}\}} |\partial \mathcal{C}_{i,\text{in},j}| \left| \mathbf{D}_{i,\text{in},j}^n \cdot \mathbf{n}_{i,\text{in},j} \right| \\ \leq 1. \tag{21}$$

Furthermore, the following results can also be established:

a) if $\Delta \text{up}_{i,\text{out}}^n < 0$, (19) is satisfied;
b) if $\Delta \text{up}_{i,\text{out}}^n > 0$, (18) is satisfied.

It thus follows, from (18) and (19), the restrictive conditions for the downwind factors can be summarized as:

$$0 \leq \lambda_{i,\text{out}}^n \leq 1; \tag{22}$$

$$0 \leq \lambda_{i,\text{in},j}^n \leq 1, \ \forall j; \tag{23}$$

$$\lambda_{i,\text{out}}^n \leq \frac{1}{|\Delta \text{up}_{i,\text{out}}^n|} \left[|\mathcal{C}_i| \, (\alpha_i^n - m_i^n) + \right. \\ \left. \sum_{j \in \{\text{in}\}} (1 - \lambda_{i,\text{in},j}^n) \Delta \text{up}_{i,\text{in},j}^n \right], \text{if } \Delta \text{up}_{i,\text{out}}^n < 0; \tag{24}$$

$$\lambda_{i,\text{out}}^n \leq \frac{1}{|\Delta \text{up}_{i,\text{out}}^n|} \left[|\mathcal{C}_i| \, (M_i^n - \alpha_i^n) - \right. \\ \left. \sum_{j \in \{\text{in}\}} (1 - \lambda_{i,\text{in},j}^n) \Delta \text{up}_{i,\text{in},j}^n \right], \text{if } \Delta \text{up}_{i,\text{out}}^n > 0. \tag{25}$$

It is certain that the system of inequalities (22)-(25) admits solutions $\{\lambda_{i,\text{out}}^n\}$ (for instance, $\lambda_{i,\text{out}}^n = 0$ is inside its solution region for any $\lambda_{i,\text{in},j}^n$). Unfortunately in (22)-(25) all the intercell boundaries are coupled. An easy way to find one solution is to determine, in each cell, the downwind factor $\lambda_{i,\text{out}}^n$ for the outlets, by supposing that the worst situation[2] occurs at the inlets. Let us consider inequality (24) for the sake of demonstration.

If we have, for the intercell inlet boundary $\partial \mathcal{C}_{i,\text{in},j}$,

$$\Delta \text{up}_{i,\text{in},j}^n > 0,$$

then the worst value of $\lambda_{i,\text{in},j}^n$ to ensure (24) is unity. On the other hand, if

$$\Delta \text{up}_{i,\text{in},j}^n < 0,$$

then the worst situation is when $\lambda_{i,\text{in},j}^n$ vanishes. These considerations lead to the worst sufficient condition for (24):

$$\lambda_{i,\text{out}}^n \leq \Lambda_i^{n,(-)}, \tag{26}$$

---

[2]In the present case, "worst situation" means the maximum downwind factor $\lambda_{i,\text{out}}^n$ to be determined with the system (22)-(25) will take its smallest value.

8

where the critical value $\Lambda_i^{n,(-)}$ reads

$$
\Lambda_i^{n,(-)} = \frac{1}{|\Delta\mathrm{up}_{i,\mathrm{out}}^n|}\Bigg[|\mathcal{C}_i|\,(\alpha_i^n - m_i^n) +
$$
$$
\sum_{j\in\{\mathrm{in}\}} \frac{1}{2}\Big(1 - \mathrm{sign}(\Delta\mathrm{up}_{i,\mathrm{in},j}^n)\Big)\Delta\mathrm{up}_{i,\mathrm{in},j}^n \Bigg], \quad (27)
$$
$$
\text{for } \Delta\mathrm{up}_{i,\mathrm{out}}^n < 0.
$$

It must be emphasized that $\Lambda_i^{n,(-)}$ in (27) can be explicitly computed, while (24) is complex to deal with since coupling all the intercell boundaries. Using the definition (8), expression (27) can be further modified into:

$$
\Lambda_i^{n,(-)} = \frac{|\mathcal{C}_i|}{|\Delta\mathrm{up}_{i,\mathrm{out}}^n|}\Bigg[\alpha_i^n\Bigg(1 - \frac{\Delta t}{|\mathcal{C}_i|}\sum_{j\in\{\mathrm{in}\}}
$$
$$
\frac{1}{2}\Big(1 - \mathrm{sign}(\Delta\mathrm{up}_{i,\mathrm{in},j}^n)\Big)|\partial\mathcal{C}_{i,\mathrm{in},j}|\,|\mathbf{D}_{i,\mathrm{in},j}^n \cdot \mathbf{n}_{i,\mathrm{in},j}|\Bigg)
$$
$$
+ \sum_{j\in\{\mathrm{in}\}} \alpha_{i,\mathrm{in},j}^n \Bigg(\frac{\Delta t}{|\mathcal{C}_i|}\frac{1}{2}\Big(1 - \mathrm{sign}(\Delta\mathrm{up}_{i,\mathrm{in},j}^n)\Big)
$$
$$
|\partial\mathcal{C}_{i,\mathrm{in},j}|\,|\mathbf{D}_{i,\mathrm{in},j}^n \cdot \mathbf{n}_{i,\mathrm{in},j}|\Bigg) - m_i^n \Bigg].
$$
$$
(28)
$$

Using the same line of idea than the one applied in (20) and (21), the critical downwind factor given by (28) can be shown to be non-negative. Keeping in mind the condition (22), the final optimized downwind factor, denoted by $\lambda_{i,\mathrm{out}}^n$, can be eventually derived and takes the following value:

$$
\lambda_{i,\mathrm{out}}^n = \min\{\Lambda_i^{n,(-)}; 1\}, \text{ for } \Delta\mathrm{up}_{i,\mathrm{out}}^n < 0. \quad (29)
$$

The case where $\Delta\mathrm{up}_{i,\mathrm{out}}^n > 0$ can be treated in the same manner. It can thus be concluded that the final result for the optimized downwind factor in the general case reads as follows:

$$
\lambda_{i,\mathrm{out}}^n = \begin{cases} \min\{\Lambda_i^{n,(-)}; 1\}, & \text{for } \Delta\mathrm{up}_{i,\mathrm{out}}^n < 0; \\[2mm] \min\{\Lambda_i^{n,(+)}; 1\}, & \text{for } \Delta\mathrm{up}_{i,\mathrm{out}}^n > 0. \end{cases}
$$
$$
(30)
$$

where $\Lambda_i^{n,(-)}$ and $\Lambda_i^{n,(+)}$ are respectively expressed as:

$$
\Lambda_i^{n,(-)} = \frac{1}{|\Delta\mathrm{up}_{i,\mathrm{out}}^n|}\Bigg[|\mathcal{C}_i|\,(\alpha_i^n - m_i^n) +
$$
$$
\sum_{j\in\{\mathrm{in}\}} \frac{1}{2}\Big(1 - \mathrm{sign}(\Delta\mathrm{up}_{i,\mathrm{in},j}^n)\Big)\Delta\mathrm{up}_{i,\mathrm{in},j}^n \Bigg], \quad (31)
$$

$$
\Lambda_i^{n,(+)} = \frac{1}{|\Delta\mathrm{up}_{i,\mathrm{out}}^n|}\Bigg[|\mathcal{C}_i|\,(M_i^n - \alpha_i^n) -
$$
$$
\sum_{j\in\{\mathrm{in}\}} \frac{1}{2}\Big(1 + \mathrm{sign}(\Delta\mathrm{up}_{i,\mathrm{in},j}^n)\Big)\Delta\mathrm{up}_{i,\mathrm{in},j}^n \Bigg]. \quad (32)
$$

2.3. High-order solution of the whole two-phase system

The solution procedure for the multi-dimensional UDCS applied to the full two-fluid system (1) remains similar to the description given in the previously published one dimensional case paper [35, Section 5.2]. In fact, scheme (14) or (15) applied to (1) expresses the idea of redistributing volume, mass, momentum and energy at a numerically diffused interface region with the global conservation condition satisfied.

When the UDCS second-order scheme is applied, the primitive variables (density, pressure, and velocity) can be reconstructed by a modified multi-dimensional Barth-Jespersen limiter (see Appendix B for a detailed description). Alternatively, when the UDCS anti-diffusive scheme is applied, the reconstruction stands for the volume fraction only because it was found the robustness of the UDCS anti-diffusive was reduced when all primitive variables were reconstructed.

In the following section devoted to the application of the proposed numerical strategy to non-reactive and reactive two-dimensional problems, a reconstruction for the volume fraction only will be retained for the non-reactive problems (shock bubble interactions) computed using both UDCS second-order scheme and UDCS anti-diffusive scheme, in order to assess the sole influence of the numerical treatment of the volume fraction evolution equation. A reconstruction for all primitive variables will be performed in the combustion test case for the UDCS second-order scheme.

Regarding time-accuracy, either a first-order Euler explicit scheme or a second-order Runge–Kutta

predictor–corrector scheme can be used with the UDCS second-order scheme. Coupling the UDCS anti-diffusive scheme with a second-order Runge-Kutta time integration was not found to yield a sufficiently robust numerical strategy. In the following section, the non-reactive shock bubble interaction problems will thus be solved using a first-order Euler explicit scheme for both the UDCS second-order and the UDCS anti-diffusive schemes. The UDCS second-order scheme will be combined with the second-order Runge-Kutta time-integration for the combustion problem, while the UDCS anti-diffusive scheme will remain applied with the first-order Euler time discretization.

3. Numerical results

This section is devoted to the application of the UDCS DEM/RDEM approach to two dimensional non-reactive and reactive interface problems computed on unstructured grids. The test cases have been selected so that they display physical features and numerical difficulties representative of those encountered for real-life applications (full reactor containment for instance). The geometries, though academic, are meshed using unstructured grids made of quadrangular and triangular elements which allow an assessment of the UDCS DEM/RDEM sensitivity to the grid topology.

The first non-reacting test case is the interaction between a shock moving through air and a bubble of heavy gas initially at rest in the surrounding air. This classical test problem for multiphase solvers has been previously computed for instance in [28, 31, 27, 3, 6, 22, 23, 37, 26]. The computed solutions obtained using UDCS and DEM will be compared to available experimental data and comments will be also provided with respect to some of the numerical results available in the literature.

The second non-reacting test problem is, again, the interaction between a shock and a bubble but the bubble is now made of a light gas and immersed in a liquid medium. This problem has been analyzed in [22] using an anti-diffusive strategy applied to a reduced two-fluid model with a single pressure and a single velocity. Note that, as a multi-D extension to the one dimensional liquid-gas interface computed in [35, Section 6.1], this two-phase shock bubble problem is made especially difficult by the very high ratio of both pressure and density between the liquid and gaseous phases. In addition, the multi-dimensional expansion wave appearing in the liquid phase may often produce negative pressures which are likely to cause in turn serious numerical difficulties. As a matter of fact, even the theoretically robust (but inaccurate) first-order upwind DEM method fails to compute this flow on triangular grids because the occurrence of a negative pressure in the liquid phase prevents from maintaining a physical sound speed (the computed quantity $c^2 = \frac{\gamma(p+p_\infty)}{\rho}$ becomes negative). The stability of the UDCS approach being that of the first-order approach, UDCS calculations can not be performed either on such triangular grids. Thus, calculations on unstructured quadrangular grids only will be performed with UDCS for this very demanding test case.

Finally, a one dimensional line-symmetric steady deflagration test problem will be computed as a demonstration reacting test-case, using UDCS and RDEM on a two dimensional quadrangular grid. The numerical results obtained will be compared with an available one dimensional reference solution. Note that, from a physical viewpoint, this reference solution for the multi-dimensional reactive Euler equations is in fact unstable since the stability of a cylindrical/spherical flame is guaranteed by the competition between thermal and species diffusion effects which are neglected in the reactive Euler equations. This inviscid solution can be used nonetheless for the sake of an analytical/numerical comparison since it can be seen as a 1D cylindrical average of the multi-dimensional solution.

3.1. Gaseous non-reacting shock bubble interaction

The present shock bubble test case is well documented, both from a numerical viewpoint (previous computational investigations have been performed in [28, 31, 22, 26]) and an experimental viewpoint (visualizations and quantitative results are provided in [19]).

The flow problem consists in simulating the impact of a Mach 1.22 shock traveling through air (light gas) onto a cylinder of R22 gas (heavy gas). The configuration is thoroughly described in Fig. 4. The cylinder of R22 gas is surrounded by air within a $445\,\text{mm} \times 89\,\text{mm}$ rectangular computational domain. At $t = 0$, the cylinder is at rest and its
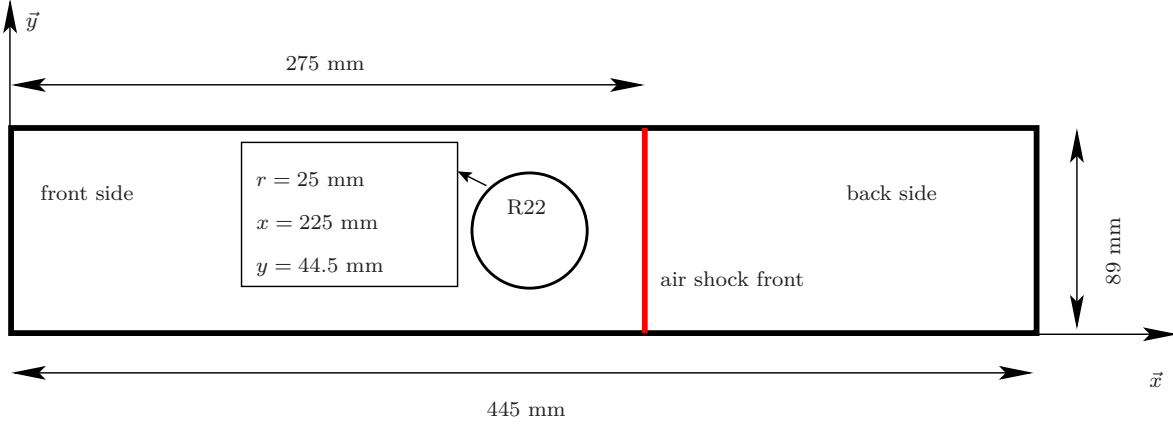
Figure 4: Initial configuration for the air-R22 shock problem.

center is located at $(x, y) = (225 \text{ mm}, 44.5 \text{ mm})$. The initial radius of the cylinder (or gas bubble) is $r = 25$ mm. The planar shock is initially located at $x = 275$ mm and moves from right to left towards the cylinder. The interaction between the material interface and the shock wave, coming from the light gas region into the heavy gas region, generates a system of waves which includes, at the early stage of the interaction, an incident shock wave in air, a refracted shock wave in the R22 bubble, a material interface and a reflected shock wave in air. Due to the smaller speed of sound in the R22 gas, the refracted shock wave in R22 propagates more slowly than the incident shock wave in air.

Both fluids (air and R22) are described by a polytropic EOS. The initial conditions and the fluid properties are summarized in Table 1. The top and bottom boundary conditions are set as solid walls while constant state boundary conditions are imposed on the left and right boundaries which are not reached by the propagating waves at the final time of the simulation.

In Fig. 5, experimental Schlieren images taken from [19] are displayed on the first column and compared with the numerical solutions provided by 2 different numerical strategies, relying on DEM and UDCS for the volume fraction equation but with a second-order approach (reconstruction with the modified Barth-Jespersen limiter) or anti-diffusive approach, each of these strategies being applied on a quadrangular or triangular grid. The presentation of the results in Fig. 5 is organized as follows:

a) column 2: UDCS second-order method with re-

construction by the modified Barth-Jespersen limiter, on a 1000×200 quadrangular mesh.

b) column 3: UDCS second-order method with reconstruction by the modified Barth-Jespersen limiter, on a $1000 \times 200 \times 2$ triangular mesh (meaning each quadrangular cell of the previous grid has been split into two triangles).

c) column 4: UDCS and anti-diffusive approach, on a 1000×200 quadrangular mesh.

d) column 5: UDCS and anti-diffusive approach, on a $1000 \times 200 \times 2$ triangular mesh.

In all cases, the Euler explicit scheme is used for time discretization, with a CFL value set to 0.4. No reconstruction on the primitive variables is performed. As done in [19], the results are displayed around the R22 gas bubble at several time instants (measured relative to the moment when the shock wave first interacts with the bubble boundary at time $t = 60$ μs). For the sake of conciseness, only a selection of the experimental snapshots has been retained but the reference used to design each instant is kept consistent with the one used in the experimental work [19], namely: (b) $t = 115$ μs, (d) $t = 187$ μs, (g) $t = 342$ μs, (h) $t = 417$ μs, (i) $t = 1020$ μs. A first qualitative analysis of the UDCS/DEM numerical results, on both triangular and quadrangular meshes, allows to conclude the computed solutions are globally in good agreement with the experimental data in [19] (and also with previous numerical results such as [28, 31, 22]). Moreover, it can be observed on the density mappings that the interface resolution is significantly improved when the UDCS anti-diffusive method is employed, be it on the quadrangular or triangular

Location	ρ (kg m^{-3})	p (Pa)	u_x (m s^{-1})	u_y (m s^{-1})	γ
Air (back side)	1.686	1.59×10^5	-113.5	0	1.4
Air (front side)	1.225	1.01325×10^5	0	0	1.4
R22	3.863	1.01325×10^5	0	0	1.249

Table 1: Air-R22 shock cylinder interaction test. EOS coefficients and initial data.
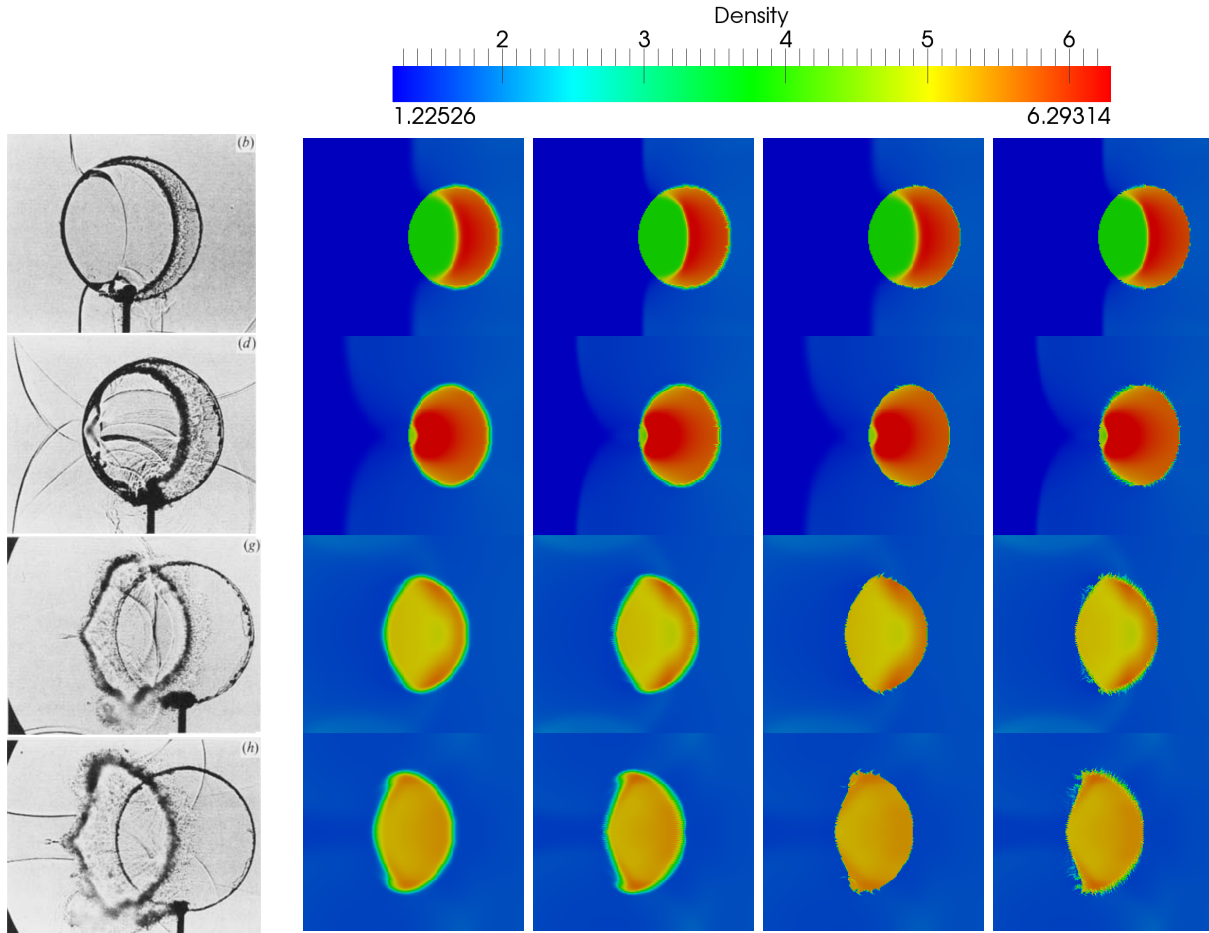
Figure 5: Air-R22 shock cylinder interaction test. Numerical results for density profile. From left to right: experimental results in [19], UDCS second-order method with 1000×200 quadrangular mesh, UDCS second-order method with triangular mesh of $1000 \times 200 \times 2$ cells, UDCS anti-diffusive method with 1000×200 quadrangular mesh, and UDCS anti-diffusive method with triangular mesh of $1000 \times 200 \times 2$ cells. Five instants are selected from [19]: (b) $t = 115$ μs, (d) $t = 187$ μs, (g) $t = 342$ μs, (h) $t = 417$ μs, (i) $t = 1020$ μs.

grid. It is in particular interesting to notice that the UDCS anti-diffusive method works well on the triangular mesh: the interface instabilities (of Richtmyer-Meshkov and Kelvin-Helmholtz type, see [27]) are clearly observed in Fig. 5 (i). The UDCS anti-diffusive approach is proved capable of resolving vortex structure and interface instability on a relatively coarse mesh while a (much) higher grid resolution would be required for many state-of-the-art methods (see for instance [27] or
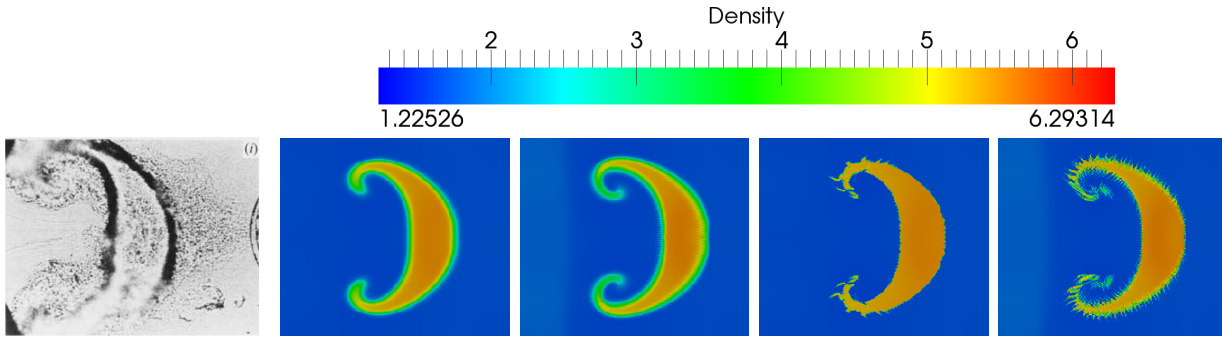
Figure 5: (*continued*)

even the more smeared interface computed using UDCS in its second-order version instead of the anti-diffusive version).

The various numerical approaches are now more quantitatively compared by analyzing the volume fraction and the mixture density at the final computational time. The results in Fig. 6 are plotted along the axis of symmetry ($+x$ direction), in the region occupied by the bubble. Three increasingly refined quadrangular meshes (250×50, 500×100, 1000×200) and three increasingly refined triangular meshes are used for accuracy comparison. Let us recall that each triangular mesh is built from the one of the quadrangular mesh by dividing each cell into two triangles so that the triangular grid is twice finer than the corresponding quadrangular mesh. On each grid, the UDCS second-order approach and UDCS anti-diffusive approach have been applied. The first line of Fig. 6 illustrates the grid-convergence of the computations performed using the UDCS anti-diffusive approach. The results displayed on the second line show that, on quadrangular grids, the UDCS anti-diffusive approach with 500×100 quadrangular mesh produces (much) more accurate results than the UDCS second-order approach with 1000×200 cells. A similar trend is observed with the triangular grids, when analyzing the results displayed on the third line: the UDCS anti-diffusive approach yields again more accurate results than the UDCS second-order approach with a crisper interface capturing.

Further plots (Fig. 8 and Fig. 9) are drawn along the two lines perpendicular to the axis of symmetry (y direction) whose location over the final time bubble shape is indicated in Fig. 7. The

grid-convergence of the results can be qualitatively observed and the UDCS anti-diffusive approach is still found to be more accurate than the UDCS second-order approach in general. For instance, in the second line of Fig. 9 for the volume fraction, the anti-diffusive method ("Anti 500×100") converges more quickly than "2-nd 500×100" in terms of both interface position and amplitude. However, with a finer mesh of "1000×200", UDCS second-order approach gives a more accurate position of the interface than "Anti 500×100". In line with the triangular mesh results displayed in Fig. 5 for the UDCS anti-diffusive approach, the interface instability is visible in the third line of Fig. 8 and Fig. 9.

The pressure time-history is displayed in Fig. 10 for the sake of comparison with [28, 31, 22, 19]. Three locations are retained: $x_p = 3$, 27, 67 mm, downstream of the R22 gas bubble along the axis of symmetry. Time is measured from the first interaction of the shock wave with the bubble at time $t = 60\ \mu s$. The UDCS anti-diffusive results on triangular grids made of $250 \times 50 \times 2$, $500 \times 100 \times 2$, and $1000 \times 200 \times 2$ elements are presented so that grid convergence can be qualitatively checked. Note that as far as the pressure time-history along the symmetry axis is concerned, no noticeable difference is observed when comparing the results obtained with the UDCS second-order method and the UDCS anti-diffusive method on the same mesh. Note also that the pressure peaks are not as accurately resolved as in [22], where a more refined (5000×1000) quadrangular grid was used. Moreover, it is worthwhile to mention that, with the same CFL value, a larger number of time steps is required for computing the flow evolution with a full non-equilibrium two-fluid flow model than with a sub-model, such as the one used in [22]
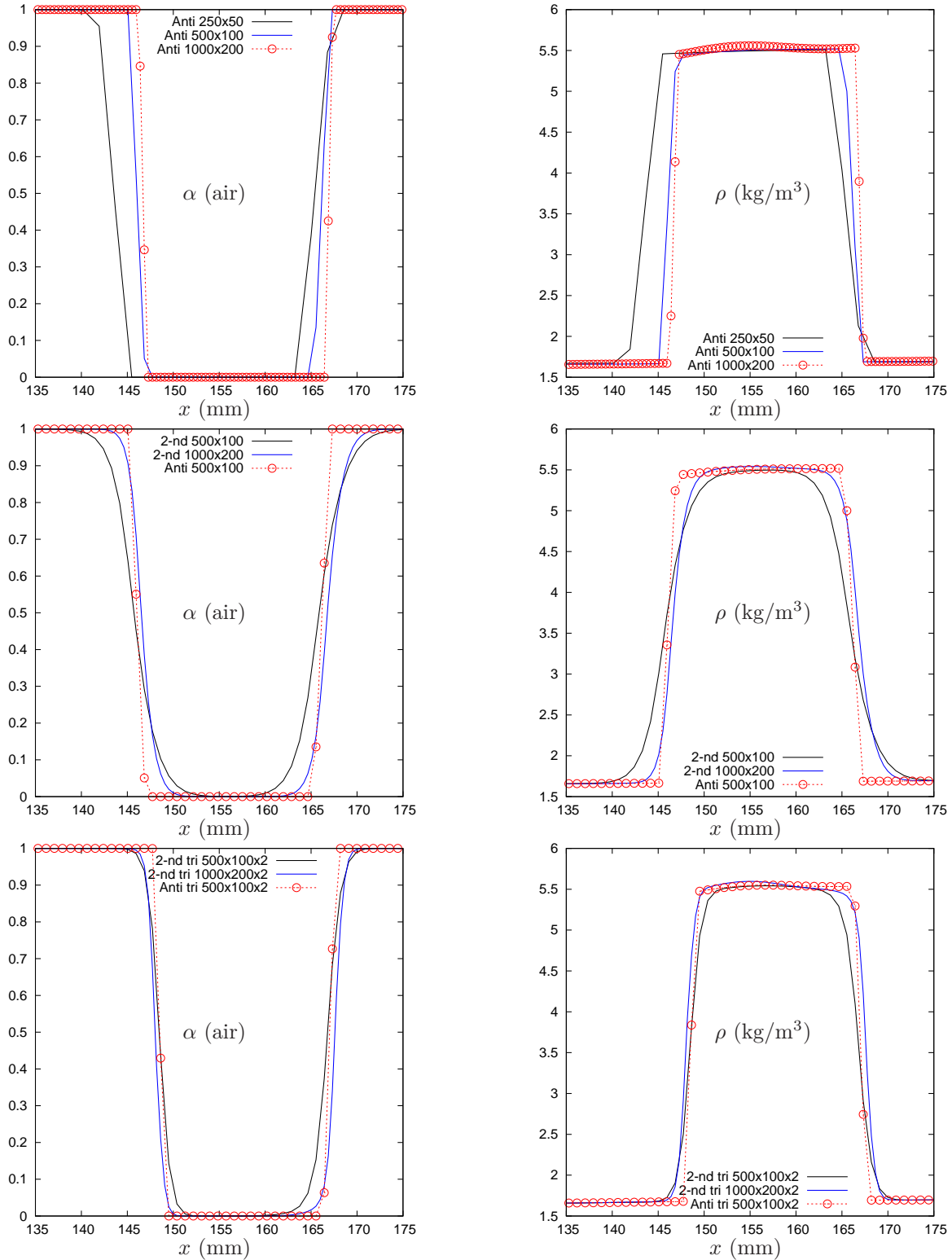
13

Figure 6: Air-R22 shock cylinder interaction test. Plots of volume fraction and mixture density over the axis of symmetry (x direction) around the R22 bubble. Anti stands for UDCS anti-diffusive approach. 2-nd stands for UDCS second-order approach. tri stands for triangular mesh.
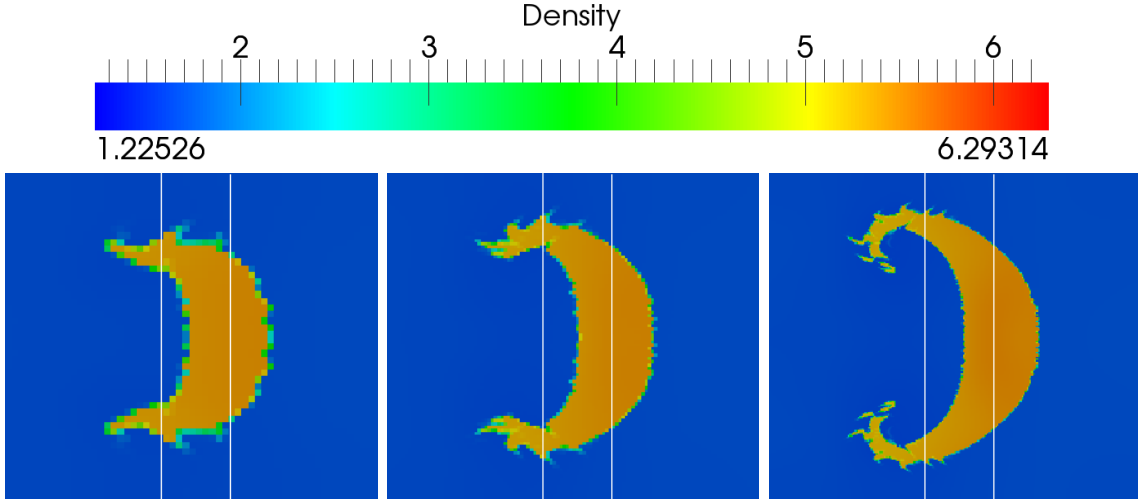
Figure 7: Air-R22 shock cylinder interaction test. Positions of y direction lines for plots of volume fraction and mixture density in Fig. 8 and Fig. 9. From left to right: UDCS anti-diffusive approach with quadrangular mesh of 250×50, 500×100, and 1000×200 cells. Left line is located at $x = 136$ mm, and right line at $x = 155$ mm (measured from the left boundary of the whole domain).

(more information can be found in [39]). This usually yields results of the full two-fluid model that are more diffused than the ones obtained with a sub-model. However, it is emphasized that the full two-fluid model must be assessed in this work since it will be necessarily used to compute reactive fronts on which the pressure and velocity jumps can be significant.

Finally, the computed characteristic wave speeds of this shock-cylinder interaction problem are measured and compared to experimental results in [19] and to numerical results in [28, 31, 22, 26]. Fig. 11 illustrates the characteristic waves that are considered in this paper: the incident shock wave ("Inc" in Fig. 11), the upwind interface wave ("Upw" in Fig. 11), the downwind interface wave ("Dow" in Fig. 11), the refracted shock wave ("Ref" in Fig. 11), and the transmitted shock waves ("Tr1" and "Tr2" in Fig. 11). The incident shock wave speed is measured at 5 mm above the bottom boundary ($y = 5$ mm), while all other waves are evaluated at the symmetry axis ($y = 45$ mm). A schematic drawing of front evolution in time-space diagram of these characteristic waves is also given in Fig. 11. The wave trajectories computed using the UDCS anti-diffusive technique are reported in Fig. 12. Note that the UDCS second-order approach gives very similar trajectories (not shown). The characteristic wave speeds estimated using a linear least-

square regression are reported tin Table 2 together with experimental results in [19] and previous simulation results in [28, 31, 22, 26]. The speed of the incident shock wave (V_s) is obtained by using 25 data points over the time-period $[0, 250]$ μs, that of the refracted shock wave (V_r) by 20 data points over $[0, 200]$ μs, and that of the transmitted shock wave (V_{t_2}, "Tr2" in Fig. 11) by 5 data points over $[200, 250]$ μs. The initial speeds of upwind and downwind interfaces (V_{ui} and V_{di}, respectively) are computed by using 40 data points over $[0, 400]$ μs and by 20 data points over $[200, 400]$ μs, respectively. Those of the final stage (V_{uf} and V_{df}) are computed by using 20 data points over $[400, 1000]$ μs. Note the time is measured from the first interaction of the shock wave with the bubble at time $t = 60$ μs. Table 2 shows the present results obtained using both UDCS second-order solver and UDCS anti-diffusive solver agree well with previous numerical studies and with the experiment.

3.2. Liquid-gas non-reacting shock bubble interaction

In this section, the two dimensional shock bubble interaction test now involves a lighter gas bubble surrounded by (heavier) liquid water. The geometry of the initial configuration is described in Fig. 13. Both fluids are thermodynamically described by the Stiffened Gas EOS ($P_\infty = 0$ for the gas). The EOS parameters and the initial fluids
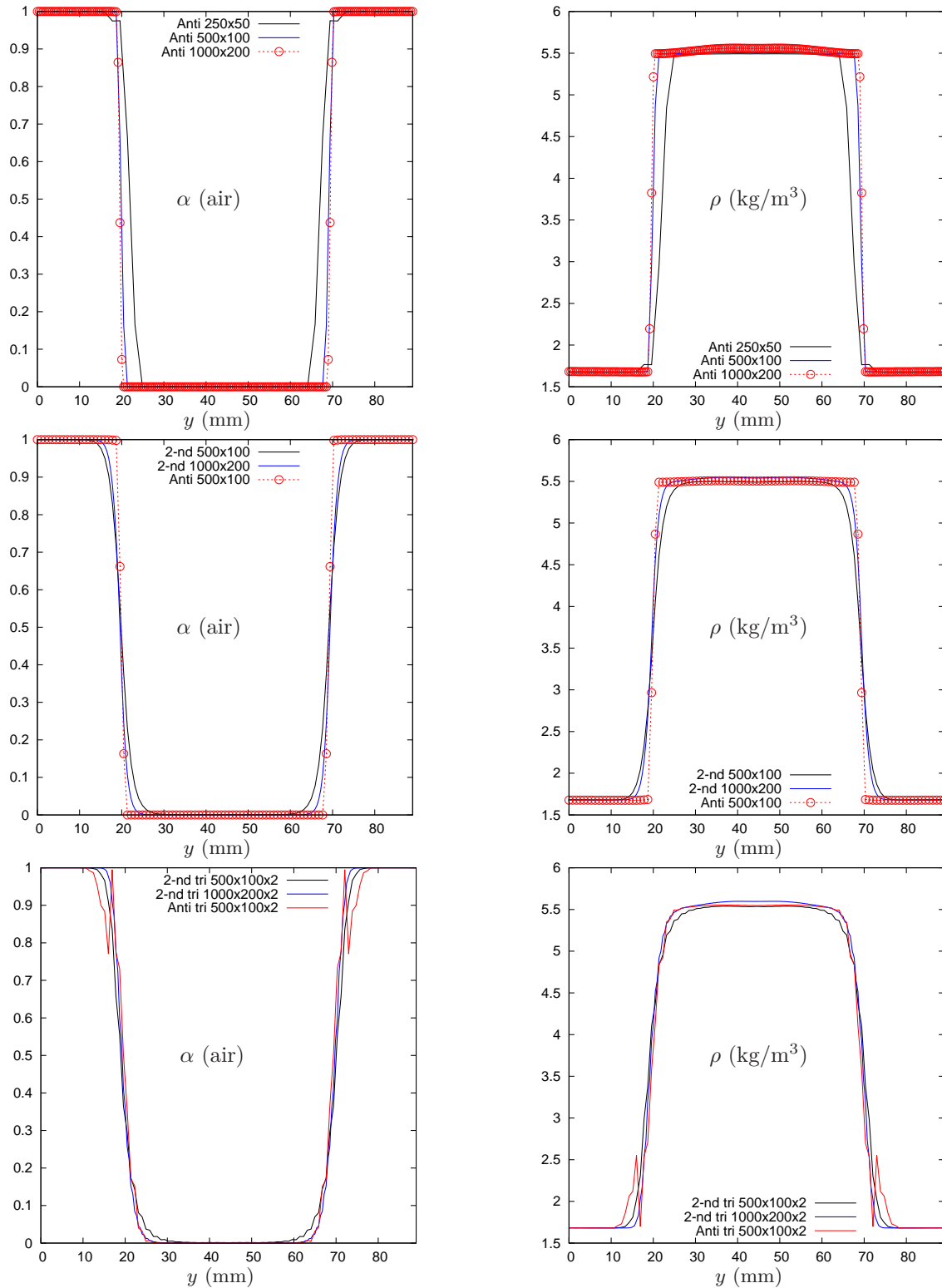
15

Figure 8: Air-R22 shock cylinder interaction test. Plots of volume fraction and mixture density over the line located at $x = 155$ mm (Fig. 7). "Anti" stands for UDCS anti-diffusive approach. "2-nd" stands for UDCS second-order approach. "tri" stands for triangular mesh.
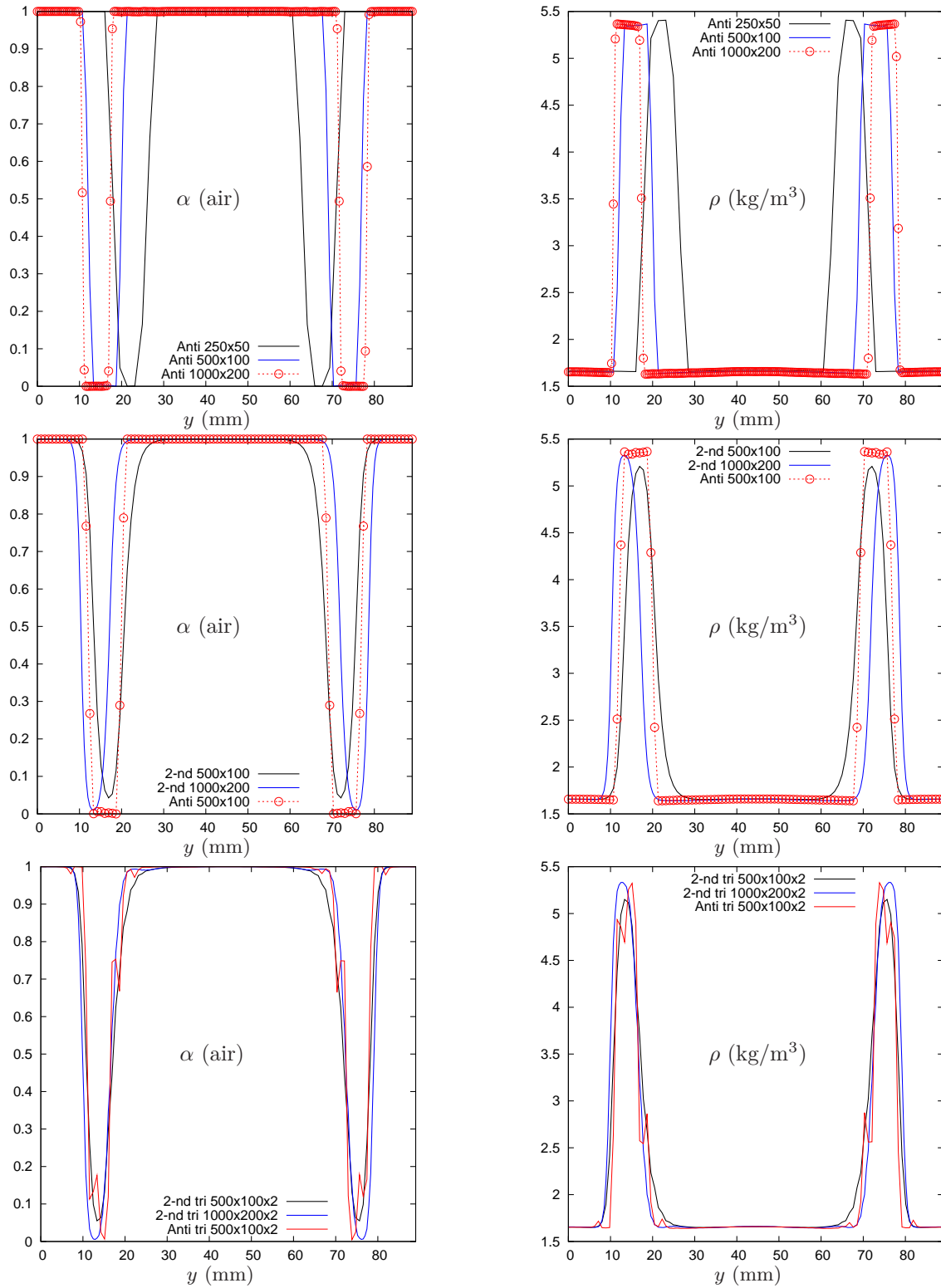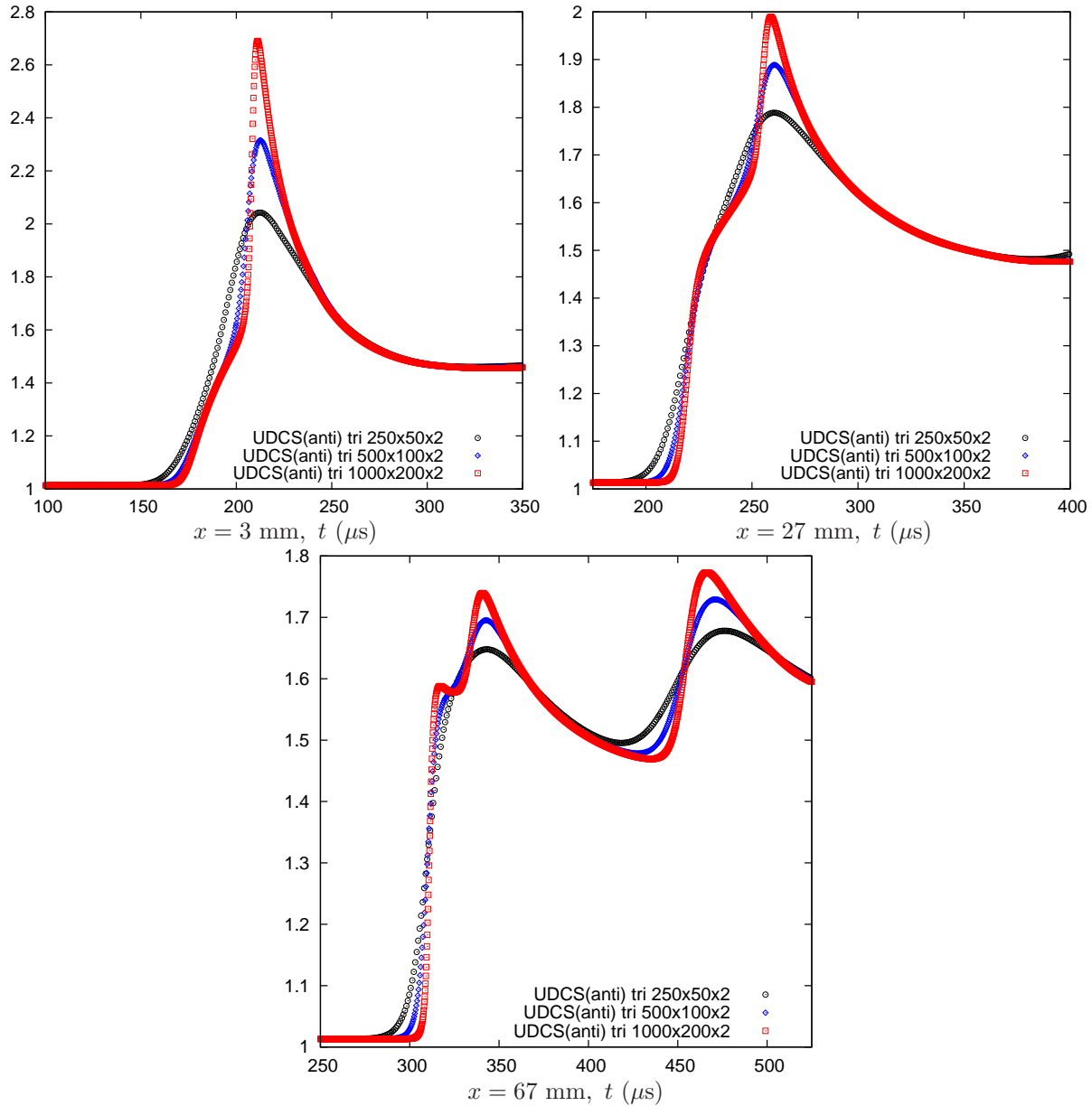
Figure 9: Air-R22 shock cylinder interaction test. Plots of volume fraction and mixture density over the line situated at $x = 136$ mm (Fig. 7). "Anti" stands for UDCS anti-diffusive approach. "2-nd" stands for UDCS second-order approach. "tri" stands for triangular mesh.

Figure 10: Air-R22 shock cylinder interaction test. Time history of pressure in three locations: $x = 3$ mm, $x = 27$ mm, and $x = 67$ mm downstream of the R22 gas bubble along the axis of symmetry. "Anti" stands for UDCS anti-diffusive approach. "tri" stands for triangular mesh.

states are given in Table 3. Solid wall boundary conditions are applied for the top and bottom boundaries while constant states are imposed at the left and right boundaries.

We underline again that this test case is very difficult because of the tremendous difference of density and pressure levels between liquid and

gas. Even the first-order DEM approach does not successfully compute this problem on a triangular mesh. Thus, the computational domain is only discretized using a 300×100 quadrangular grid. The first-order Euler method is used for time discretization.

Fig. 14 and Fig. 15 display the computed solu-

18
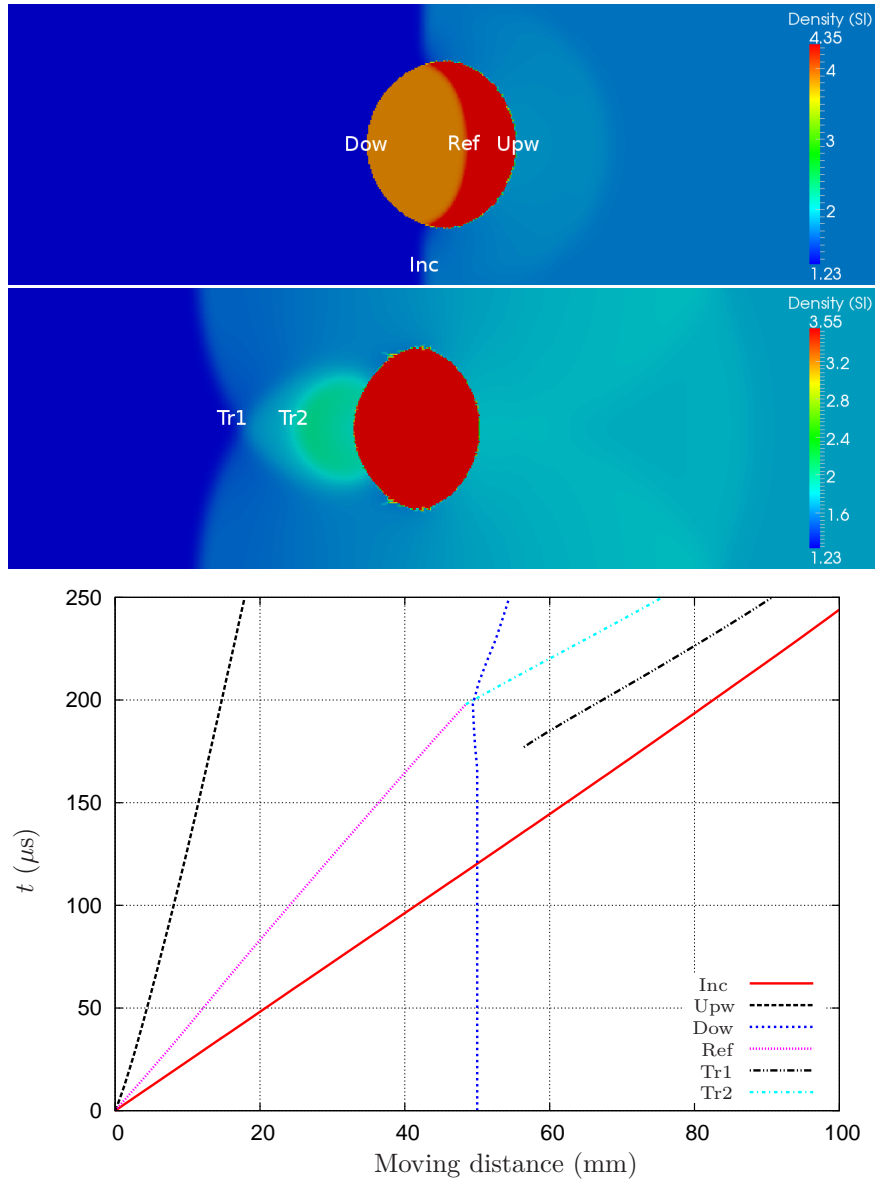
Figure 11: Air-R22 shock cylinder interaction test. Top: schematic view of the characteristic waves, namely the incident shock wave ("Inc"), the upwind interface wave ("Upw"), the downwind interface wave ("Dow"), the refracted shock wave ("Ref"), and the transmitted shock waves ("Tr1" and "Tr2"). Bottom: evolution of the characteristic waves in the time-space diagram. The space measurement refers to the distance between the wave front and the first contact position between the bubble and the incident shock wave ($x = 250$ mm). The time is measured from the first interaction of the shock wave with the bubble at time $t = 60$ μs.

tions (volume fraction and mixture density) using UDCS and DEM at four time instants. The gas bubble is transformed into two symmetrical vortices at the end of the computational period, as also observed in [30, 22]. Compared to the second-order scheme, the UDCS anti-diffusive approach yields a much sharper interface profile. This can be fur-

ther (quantitatively) verified by visualizing volume fraction and mixture density distributions along the axis of symmetry; such distributions are plotted in Fig. 16 at time $t = 375$ μs and in Fig. 17 at $t = 450$ μs. This latter time instant corresponds to the time at which the numerically diffused interface computed with the UDCS second-order ap-

19
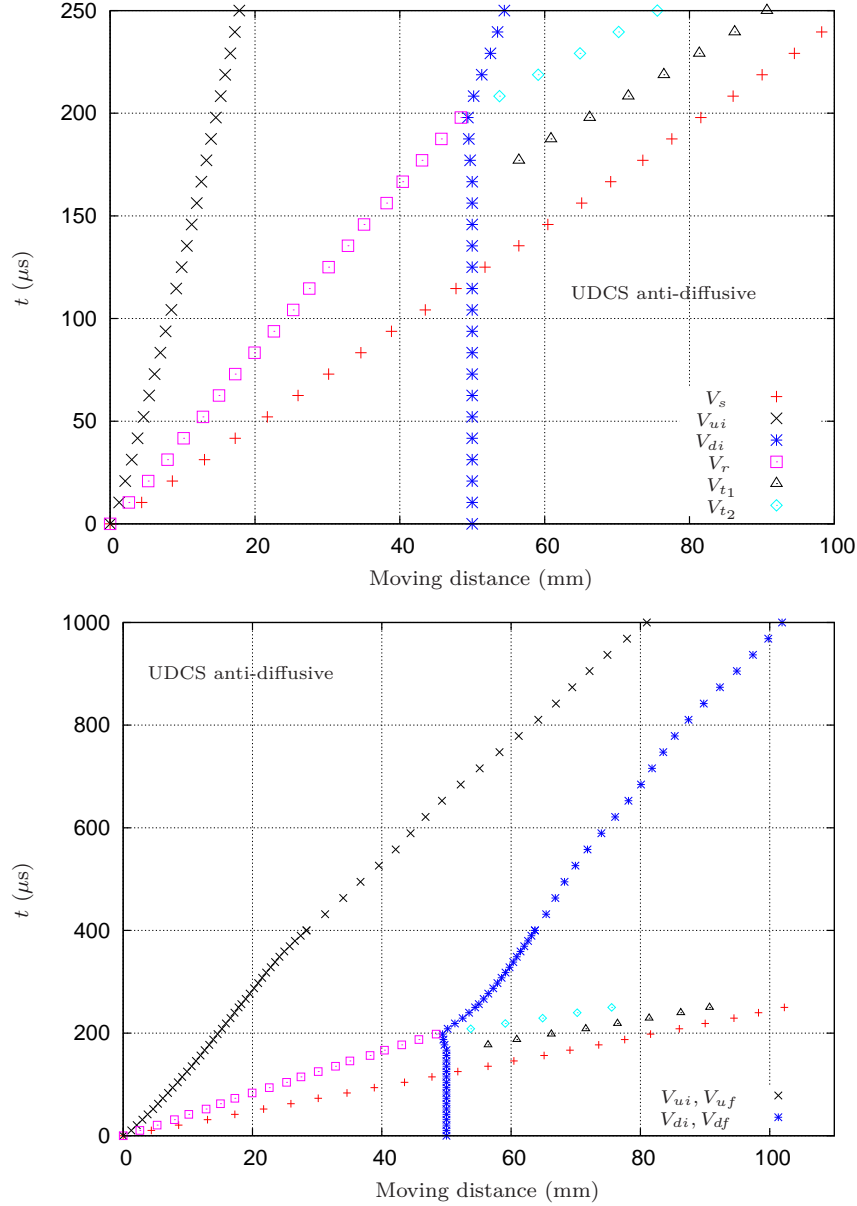
Figure 12: Air-R22 shock cylinder interaction test. DEM + UDCS anti-diffusive solver is used. The trajectories of the following characteristic waves are plotted in the time-space diagram: the incident shock wave (V_s), the upwind interface wave (V_{ui} and V_{uf} for initial and final stages, respectively), the downwind interface wave ($V_{di}$ and V_{df} for initial and final stages, respectively), the refracted shock wave (V_r), and the transmitted shock waves (V_{t_1} and V_{t_2}). The space measurement refers to the distance between the wave front and the first contact position between the bubble and the incident shock wave ($x = 250$ mm). The time is measured from the first interaction of the shock wave with the bubble at time $t = 60$ μs. Top: small time; Bottom: large time (compared to [19]).

proach interacts with the front side of the bubble. The sharper interface computed with the UDCS anti-diffusive approach is well demonstrated. At $t = 450$ μs, the anti-diffusive and second-order approaches start to yield significant difference for the pressure and density distributions along the symmetry axis; in particular, the UDCS anti-diffusive method predicts a higher pressure in the bubble zone while the UDCS second-order method tends to underestimate this pressure level.

20

Velocity (m/s)	V_s	V_r	V_{t_2}	V_{ui}	V_{uf}	V_{di}	V_{df}
Experiment [19]	415	240	540	73	90	78	78
Quirk and Karni [28]	420	254	560	74	90	116	82
Shyue (tracking) [31]	411	243	538	64	87	82	60
Shyue (capturing) [31]	411	244	534	65	86	98	76
Kokh and Lagoutière (upwind) [22]	411	243	524	66	86	83	62
Kokh and Lagoutière (anti-diffusive) [22]	411	243	525	65	86	85	64
Nonomura et al. (MUSCL) [26]	411	244	530	63	87	103	76
Nonomura et al. (Hyperbolic tangent interpolation, $\beta = 2.0$ and $\chi = 2.0$) [26]	411	243	536	64	86	98	77
DEM + UDCS(second-order) (present paper)	411	244	525	68	87	68	64
DEM + UDCS(anti-diffusive) (present paper)	411	243	525	67	87	68	64

Table 2: Air-R22 shock cylinder interaction test. The computed characteristic wave speeds are compared with experimental measurements [19] and with previous numerical studies [28, 31, 22, 26]. The following fronts are considered: the incident shock wave (V_s), the refracted shock wave (V_r), the transmitted shock wave (V_{t_2}), the upwind interface wave (V_{ui} and V_{uf} for initial and final stages, respectively), and the downwind interface wave (V_{di} and V_{df} for initial and final stages, respectively).
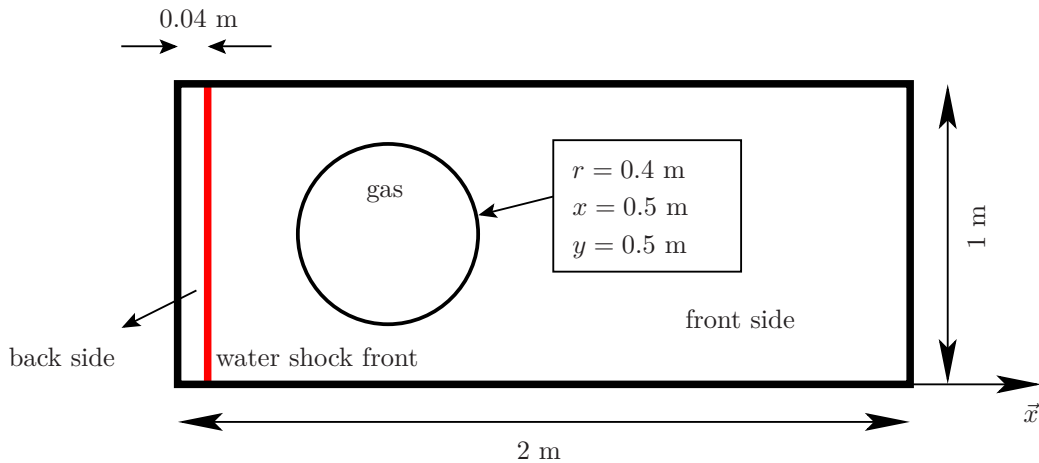
Figure 13: Initial configuration for the liquid-gas shock tube problem [22].

Location	ρ (kg m^{-3})	p (Pa)	u_x (m s^{-1})	u_y (m s^{-1})	γ	P_∞ (Pa)
Water (back)	1030.9	3×10^9	300.0	0	4.4	6.8×10^8
Water (front)	1000.0	10^5	0	0	4.4	6.8×10^8
Air	1.0	10^5	0	0	1.4	0

Table 3: liquid-gas shock bubble interaction test. EOS coefficients and initial data.
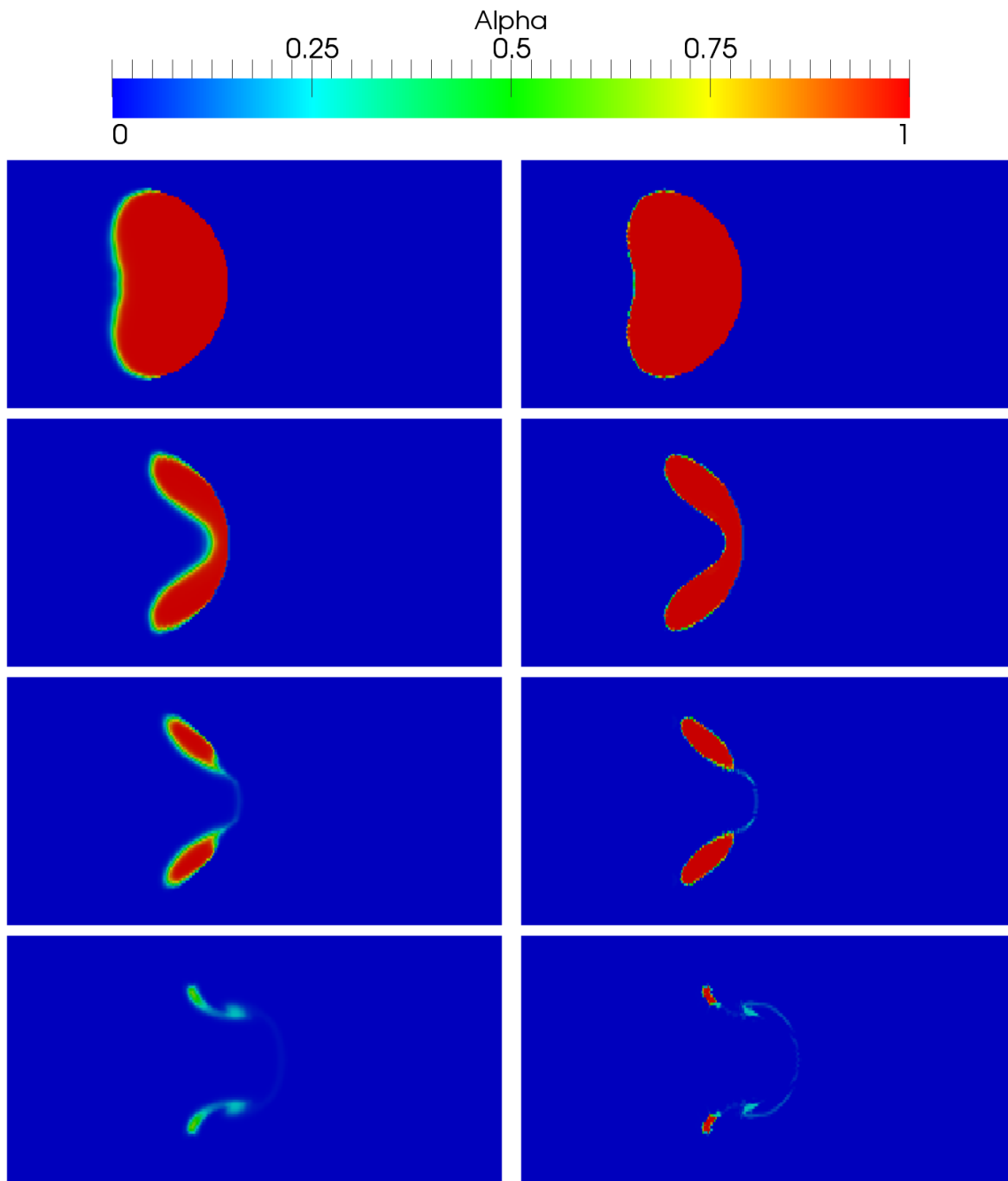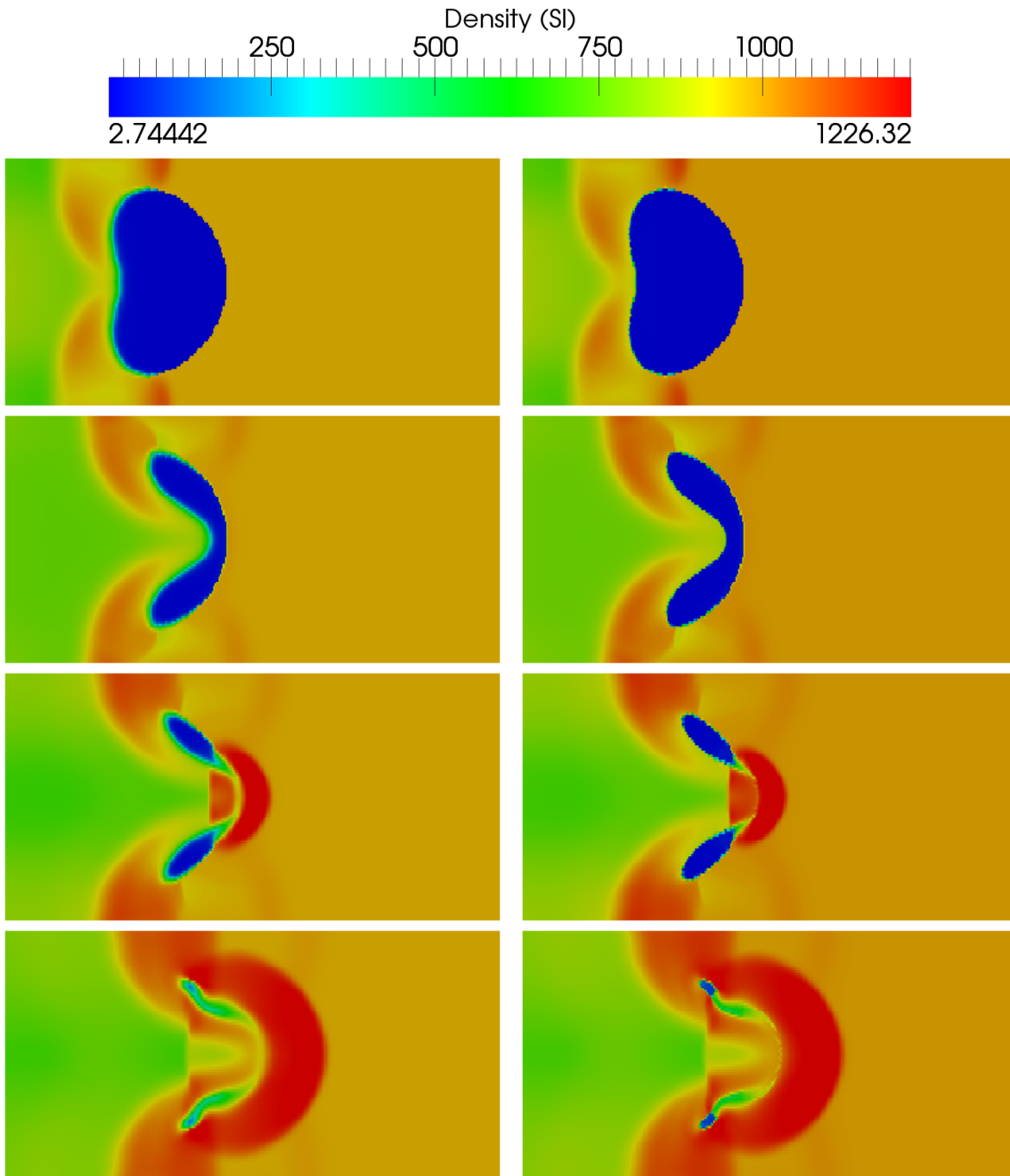
Figure 14: Liquid-gas shock bubble interaction test. Contours of the gas volume fraction. On the left: UDCS second-order DEM scheme; on the right: UDCS anti-diffusive DEM scheme. Four instants from top to bottom: $t = 225\ \mu s$, $375\ \mu s$, $450\ \mu s$, $600\ \mu s$.

3.3. 2D computation of 1D line-symmetric steady combustion

This test case has been previously considered in [4, Section 6.3, pp. 300–303]. A 2D (theoretically) unbounded domain is filled with a stoichiometric mixture of (thermally perfect) hydrogen-air at rest. At $t = 0$, combustion is initiated in a single point (the lower left corner of the computational

22

Figure 15: Liquid-gas shock bubble interaction test. Contours of the mixture density. On the left: UDCS second-order DEM scheme; on the right: UDCS anti-diffusive DEM scheme. Four instants from top to bottom: $t = 225\ \mu s$, $375\ \mu s$, $450\ \mu s$, $525\ \mu s$.

domain) and the test case studies the propagation of the 1D line-symmetric deflagration wave thus generated.

The computational domain is a square of side-length equal to $1\,\mathrm{m}$, discretized with a regular grid of 400×400 quadrangles; the CFL number is set equal to 0.4. As far as initial conditions are concerned, initial pressure and temperature are assumed respectively equal to 1.013 bar and 290 K. The fundamental speed is given by $K_0 = 45.2$ m/s. The combustion is "numerically
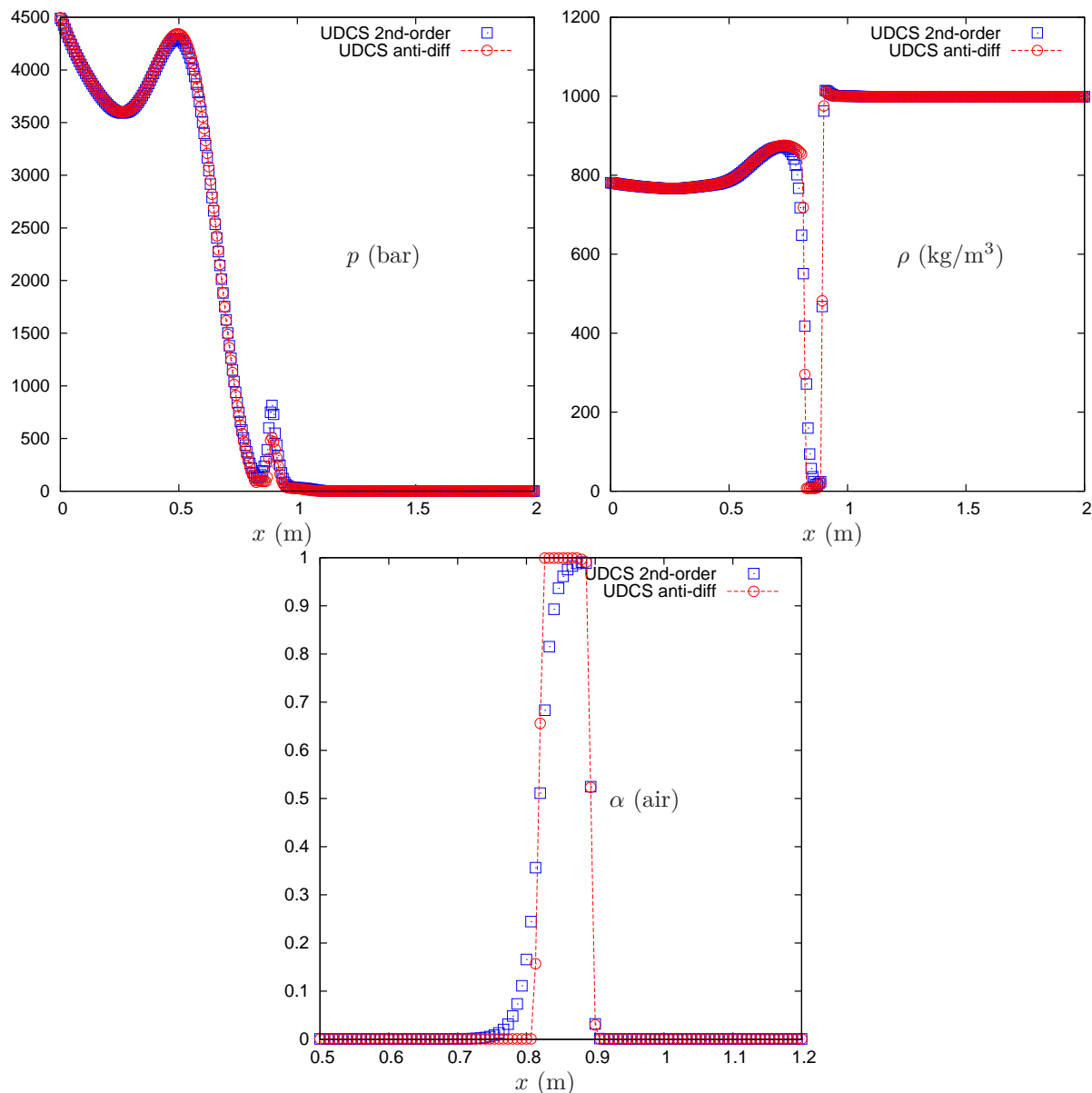
Figure 16: Liquid-gas shock bubble interaction test. Plots of pressure, density and air volume fraction over the axis of symmetry (x direction) at time $t = 375$ μs.

initiated" by supposing that the hydrogen-air mixture is burnt in the closest element to the center of symmetry (the left bottom corner of the square domain here considered). The initial pressure and temperature of the burnt gas mixture are equal to 2.013 bar and 2800 K respectively.

An accurate solution of this problem can be obtained by integrating an ordinary differential equation, as done in [24]. Alternatively, a reference

solution can be obtained by performing a 1D line-symmetric computation (as done here) and offers therefore a point of reference for the numerical results computed using the UDCS anti-diffusive approach and RDEM. As previously mentioned, this solution is not physically meaningful since diffusion effects should be necessarily included for a realistic description of a cylindrical/spherical flame (as pointed out in Borghi [5], a flame front with zero thickness is bound to be unsta-
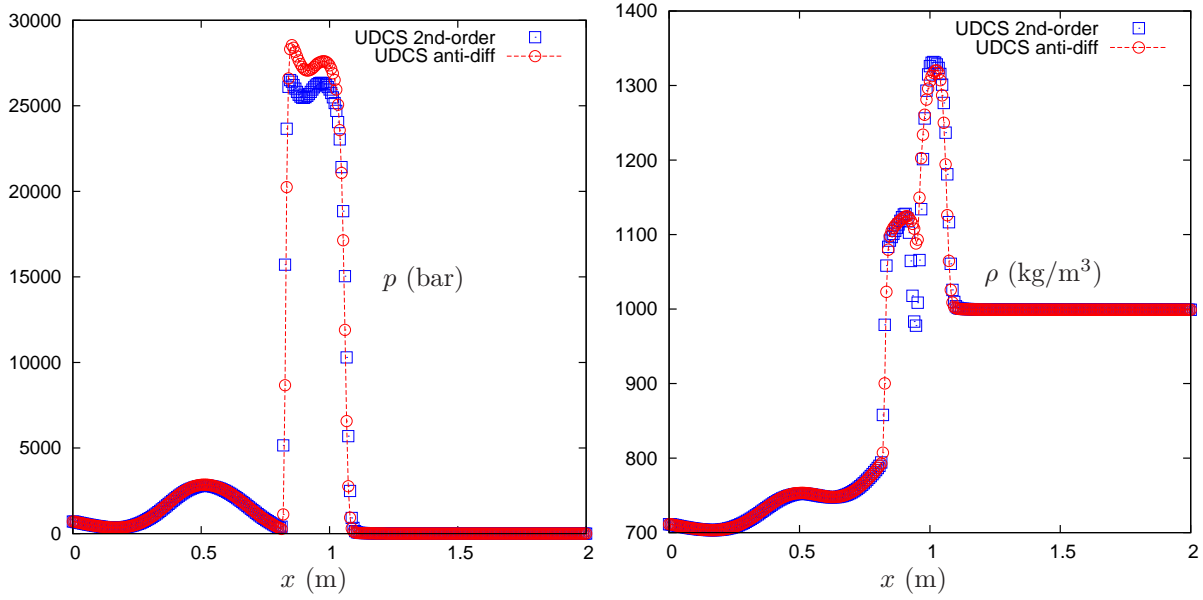
Figure 17: Liquid-gas shock bubble interaction test. Plots of pressure and density over the axis of symmetry (x direction) at time $t = 450$ μs.

ble). Still, this solution remains a valid point of reference for the present inviscid computed solutions. From now on, the 1D line-symmetric solution will be referred to as the "reference solution".

In Fig. 18-20 the computed solution at 1.2 ms is reported for different numerical strategies: the original first-order RDEM approach (explicit Euler scheme for time discretization), the (RDEM) UDCS approach with second-order reconstruction on pressure, density, velocity and volume fraction (second-order explicit Runge-Kutta scheme for time discretization), and the (RDEM) UDCS anti-diffusive approach (explicit Euler scheme for time discretization). For each method, the contours of the volume fraction of the burnt gas and the pressure are respectively displayed on the left and right pictures of the top line. On the bottom line, the density (left) and pressure (right) distributions computed along the x-axis and the diagonal ($x = y$) of the computational domain are displayed. The distributions, extracted from the 2D solutions, are also compared with the reference 1D computation. Before analyzing the various numerical solutions, it should be pointed out that, whatever the method used, the flame propagates at different speeds along the diagonal and along the axis of the domain. Such a phenomenon was already observed in [4], where the solution was obtained using the original RDEM

on a quadrangular regular mesh. In our opinion, using the original RDEM approach, this behavior was due to the fact that, when studying 1D reactive Riemann problems at the intercell boundaries, the cell interface normal $\mathbf{n}_{\text{cell}}$ can be different from the flame surface normal. Let us recall that the total flame velocity [4] is

$$\mathbf{D}_I = \mathbf{v}^{\text{unburnt}} + K_0 \mathbf{n}_{\text{flame}}$$

where $\mathbf{v}^{\text{unburnt}}$ is the cold gas velocity in front of the flame interface, K_0 the scalar fundamental flame speed, and $\mathbf{n}_{\text{flame}}$ the flame surface normal. Here $\mathbf{n}_{\text{flame}}$ is computed with the formula

$$\mathbf{n}_{\text{flame}} = \frac{< \nabla \alpha >}{| < \nabla \alpha > |},$$

where $< \nabla \alpha >$ is the numerical gradient of the volume fraction (see Appendix B for its evaluation). As shown in [4], if the fundamental flame speed is supposed to be given by

$$K_0 |\mathbf{n}_{\text{flame}} \cdot \mathbf{n}_{\text{cell}}|,$$

instead of

$$K_0 |\mathbf{n}_{\text{cell}}| = K_0,$$

when evaluating the solution of the 1D reactive Riemann problem, directional effects are drastically reduced though they do not disappear. This can be
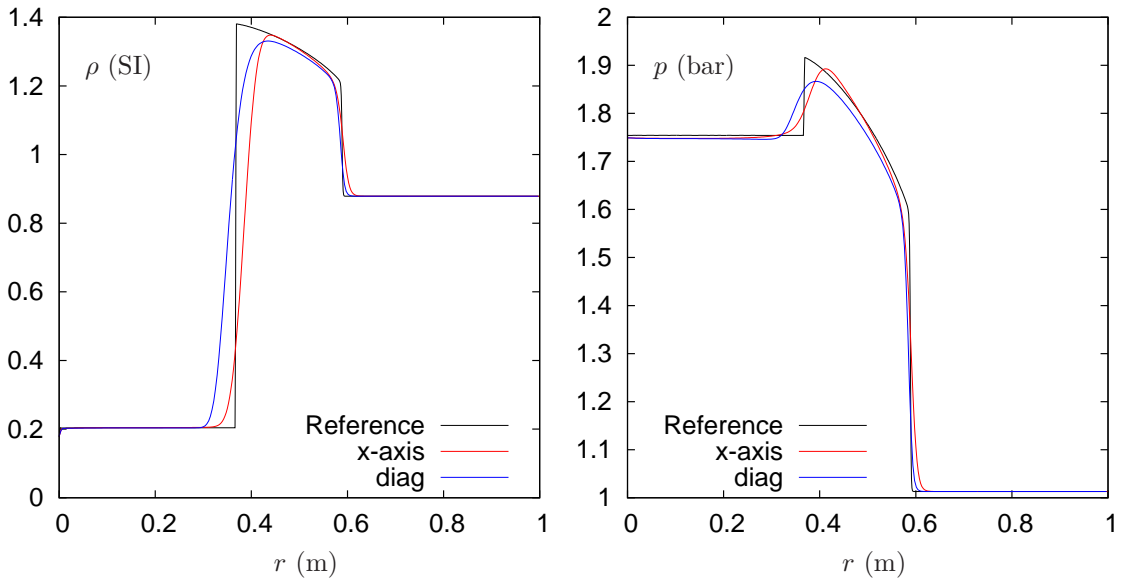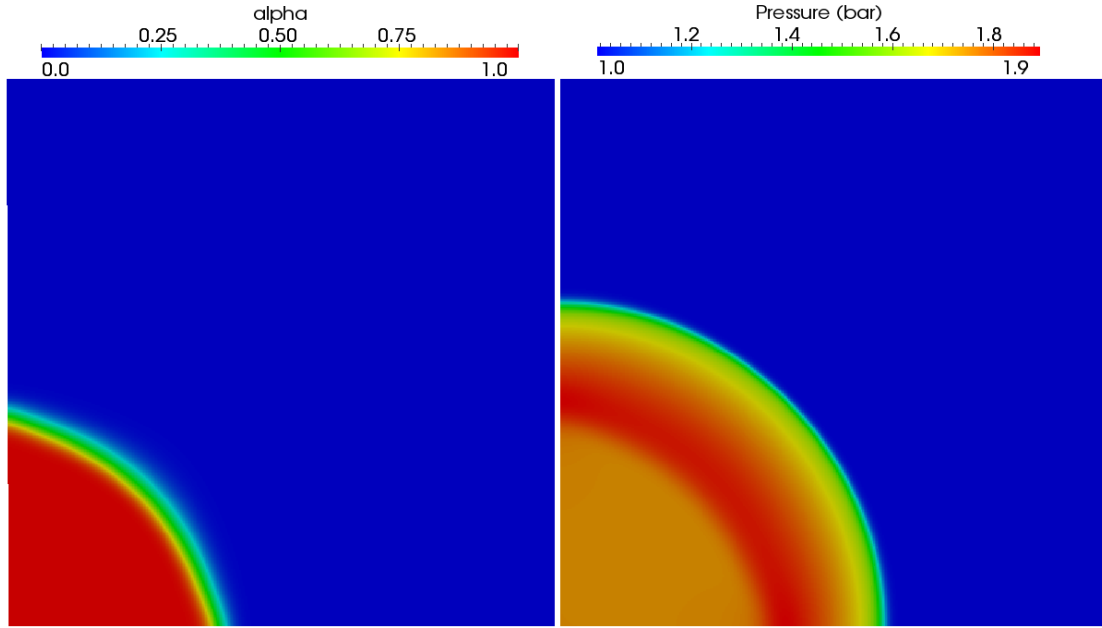
Figure 18: Propagation of a 1D line-symmetric steady flame. First-order RDEM (explicit Euler scheme for time discretization). Top: volume fraction of the burnt gas and pressure. Bottom: density and pressure plots along the axis and the left-to-right diagonal. The reference solution is obtained using a 1D line-symmetric solver and the UDCS anti-diffusive approach.

explained as follows. If the normal to the inter-cell boundary and the normal to the flame are not aligned, the solution of the reactive Riemann problem at the interface is modified. For instance, a detonation ($K_{0,\text{det}}$ given by the merging of the precursor shock and the reactive shock in the flame frame) becomes a deflagration because of the scalar product $|\mathbf{n}_{\text{flame}} \cdot \mathbf{n}_{\text{cell}}|$ which reduces the value of the fundamental flame speed. That is, instead of using a detonation fundamental flame speed

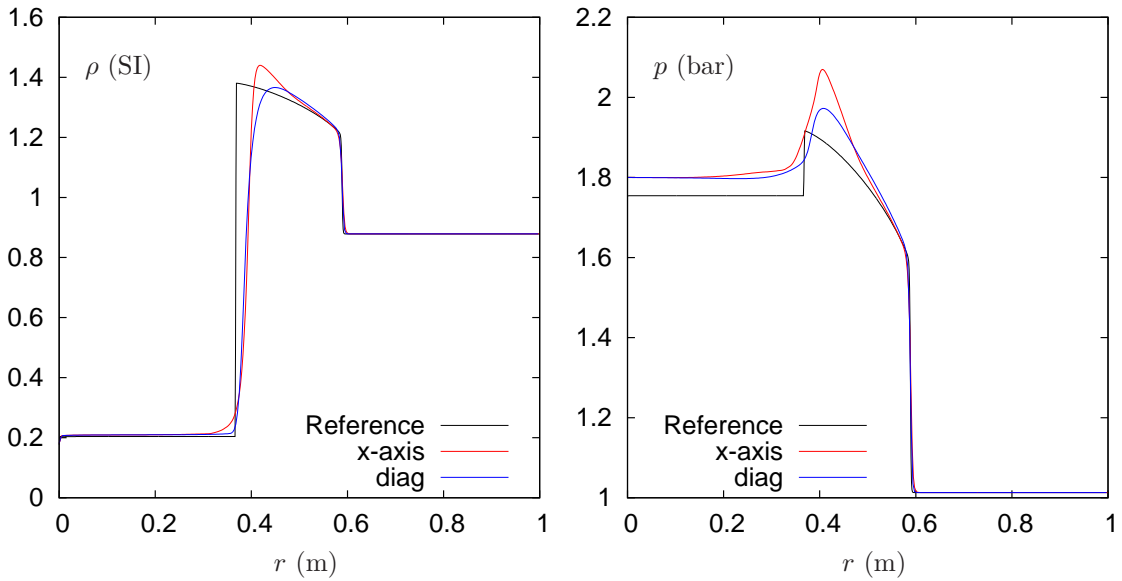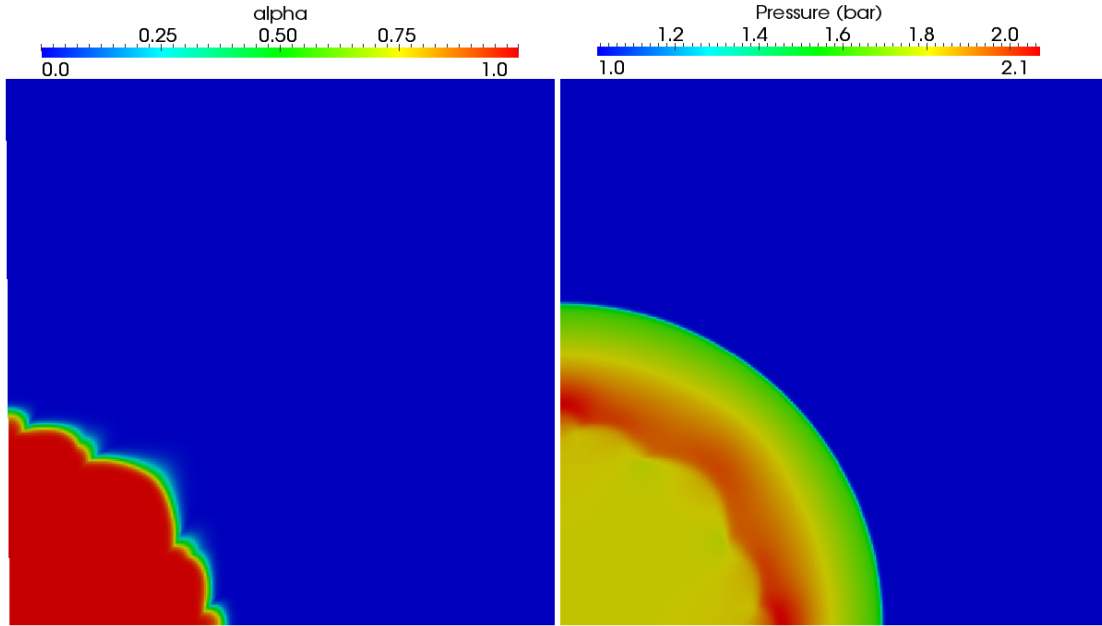$$K_{0,\text{det}} |\mathbf{n}_{\text{flame}}| = K_{0,\text{det}},$$

Figure 19: Propagation of a 1D line-symmetric steady flame. (Quasi) second-order UDCS + RDEM, with limited reconstruction (by the modified Barth-Jespersen limiter) for all primitive variables (second-order explicit Runge-Kutta scheme for time discretization). Top: volume fraction of the burnt gas and pressure. Bottom: density and pressure plots along the axis and the left-to-right diagonal. The reference solution is obtained using a 1D line-symmetric solver and the UDCS anti-diffusive approach.

one is actually using a deflagration speed:

$$K_{0,\text{det}}|\mathbf{n}_{\text{flame}} \cdot \mathbf{n}_{\text{cell}}| \to \text{deflagration.}$$

Numerical experiments (not reported here) for different values of K_0, from fast deflagration to detonation, on cylindrical and spherical flows have shown that the numerical solution, even though not converging to the exact solution, remains
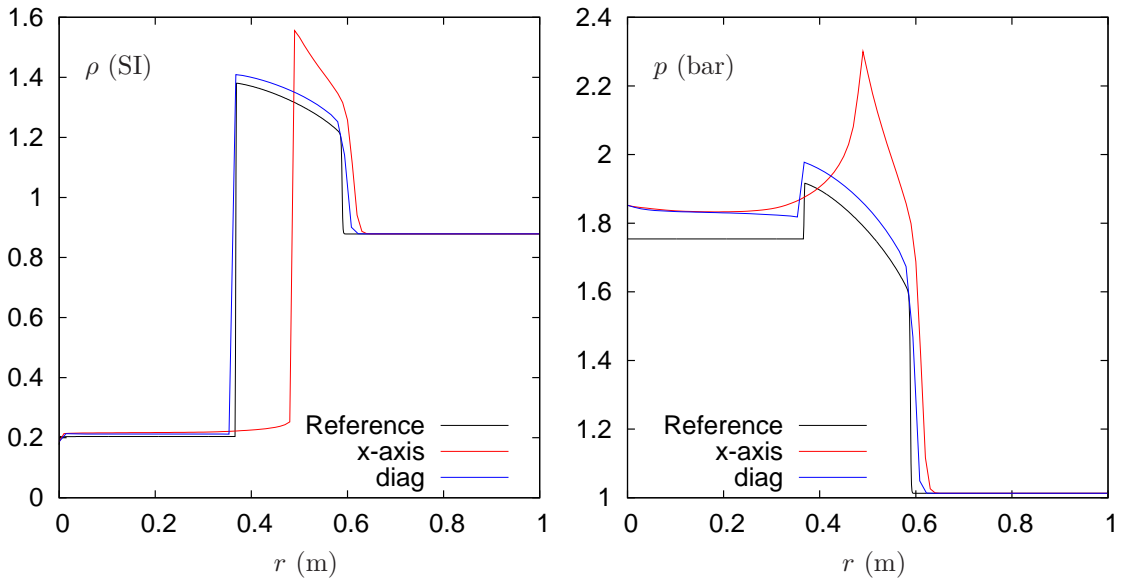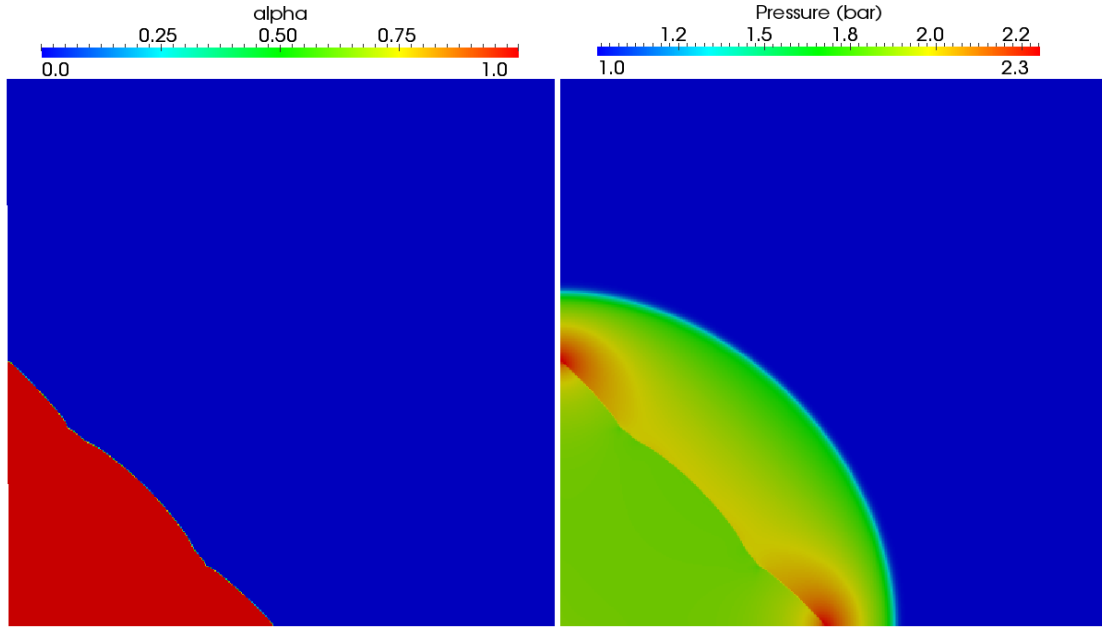
Figure 20: Propagation of a 1D line-symmetric steady flame. UDCS anti-diffusive + RDEM approach (explicit Euler scheme for time discretization). Top: volume fraction of the burnt gas and pressure. Bottom: density and pressure plots along the axis and the left-to-right diagonal. The reference solution is obtained using a 1D line-symmetric solver and the UDCS anti-diffusive approach.

acceptably close to it for the targeted applications (computed pressure waves are slightly higher than the exact ones but this can be considered as normal since due to the reactive wave instability). Since this directional effects issue is related to the RDEM framework itself, let us proceed nonetheless with the assessment of UDCS. In what follows, the normal to the flame interface is computed with the formula $\mathbf{n}_{\text{flame}} = \frac{<\nabla\alpha>}{|<\nabla\alpha>|}$ and $K_0|\mathbf{n}_{\text{flame}} \cdot \mathbf{n}_{\text{cell}}|$ defines the fundamental flame speed.

28

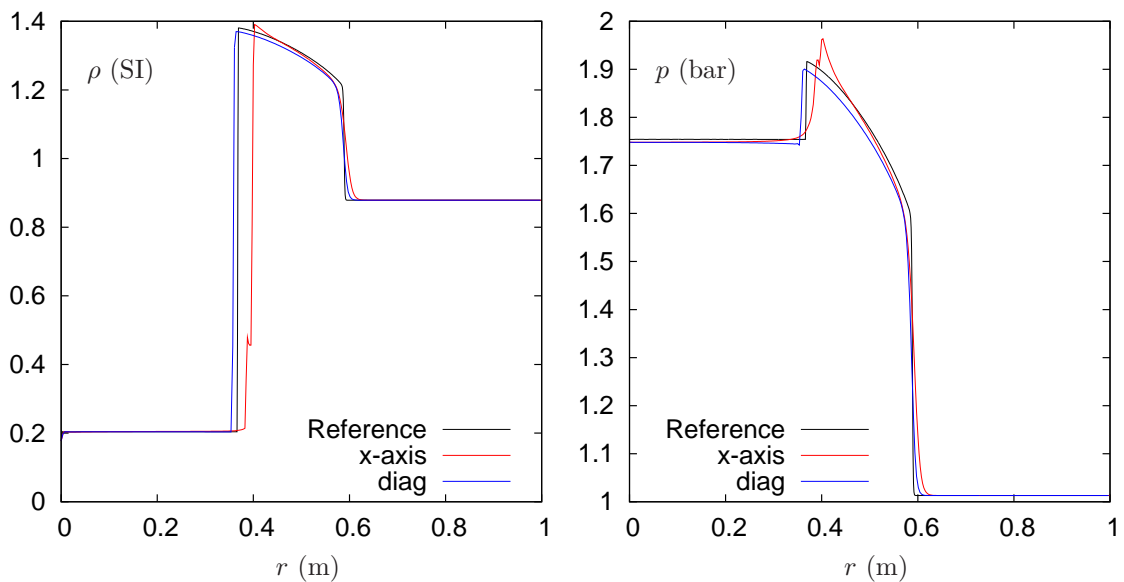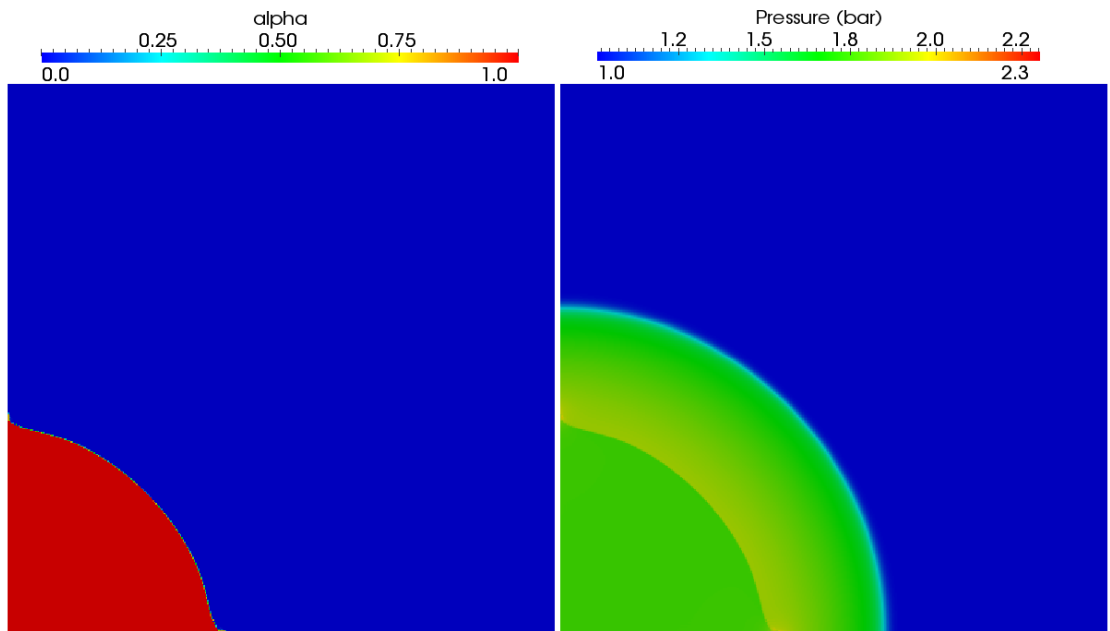Figure 21: Propagation of a 1D line-symmetric steady flame. UDCS anti-diffusive + RDEM approach (explicit Euler scheme for time discretization), in which normals at the flame interface are forced to be equal to the ones of the reference solution (namely $\mathbf{n}_{\text{flame}} = (x/r, y/r)$). Top: volume fraction of the burnt gas and pressure. Bottom: density and pressure plots along the axis and the left-to-right diagonal. The reference solution is obtained using a 1D line-symmetric solver and the UDCS anti-diffusive approach.

As can be observed in Fig. 18-20 , the numerical results in closest agreement with the reference solution are those given in Fig. 18 by the first-order

RDEM (displaying the highest numerical diffusion). The results obtained in Fig. 19 using UDCS with second-order reconstruction and RDEM are less diffused than the ones given by the first-order recon-

struction, with the propagation speed of the flame along the axis and the diagonal remaining almost the same. The flame interface shape is not circular; this is expected since the reference solution is unstable. The pressure level in the burnt gas appears higher than the one given by the first-order approach. This is due to the fact that as the flame surface wrinkles, the quantity of unburnt gas which burns per time unit increases. This phenomenon increases in turn the release of chemical energy per time unit and thus the pressure. Finally, in the UDCS anti-diffusive solution displayed in Fig. 20, it can be noticed that the volume fraction is less diffused than in the other solutions but the flame is much faster on the axis than on the diagonal. The reason for this behavior can be traced back to the flame interface normal evaluation with the formula $\frac{<\nabla\alpha>}{|<\nabla\alpha>|}$; while this expression works well as long as α is smooth enough, it tends to yield spurious normal estimates when applied with very sharp interfaces, such as the ones produced by the UDCS approach. In order to distinguish between the front capturing properties of the UDCS anti-diffusive approach and the numerical flame propagation issue, a last set of results was obtained using RDEM and UDCS anti-diffusive approach with the flame interface normal artificially set equal to the normal computed from the 1D line-symmetric solution (namely $\mathbf{n}_{\text{flame}} = (\frac{x}{r}, \frac{y}{r})$). As observed in Fig. 21, the propagation velocities are almost the same in all directions in that case and the solution remains less diffused than in the other approaches (first-order RDEM and RDEM with UDCS second-order approach), as expected.

3.4. Concluding remarks on numerical results

The UDCS anti-diffusive approach was found to yield a higher to much higher resolution of both non-reactive and reactive material interfaces with respect to the resolution provided by the UDCS second-order approach. This improved accuracy for the anti-diffusive strategy was achieved with no restriction on stability with respect to the limited second-order approach. It was also noticed that the UDCS anti-diffusive approach is in fact more efficient than the second-order limited method. As already mentioned in [35], this better overall efficiency comes from the reduced number of two-phase (non-reactive or reactive) Riemann problems which have to be solved in the DEM/RDEM framework when the material interface is numerically less

diffused thanks to the UDCS anti-diffusive strategy.

4. Conclusions & perspectives

Following the previous work [35] where a UDCS scheme has been combined with the (Reactive) Discrete Equations Method (DEM/RDEM) to compute with second-order accuracy and a very good efficiency one dimensional non-reacting and reacting two-fluid flows, the present contribution has described the multi-dimensional extension of this DEM/RDEM UDCS approach on general unstructured meshes and has applied this approach to several 2D demanding test problems for non-reacting (gaseous and liquid-gas shock bubble interactions) and reacting (combustion fronts) two-fluid flows. Note the added value of the proposed strategy, when compared for instance to [22], lies in its ability to successfully deal with permeable fronts, particularly all speed reactive fronts in the targeted applications, via the reactive Riemann solver for Euler equations.

The superior accuracy achieved with the anti-diffusive version of UDCS, be it with DEM or RDEM, with respect to a baseline second-order UDCS DEM/RDEM approach has been initially demonstrated for 1D problems in [35] and clearly confirmed in the present contribution for 2D flows corresponding to a large spectrum of physical conditions.

The DEM/RDEM UDCS approach also offers attractive robustness properties. Indeed, the UDCS approach (either limited second-order or anti-diffusive) with DEM/RDEM is proved as stable as the first-order DEM/RDEM version with piecewise constant volume fractions. This property results from the two-step strategy involved in UDCS: the first "upwind" step fully contains the first-order upwind DEM/RDEM approach, which takes into account all first-order wave propagations, including in particular the genuinely nonlinear waves; the second "downwind-controlled splitting" step aims at improving the accuracy of the linearly degenerate wave (*i.e.*, the contact discontinuity for non-reacting Stiffened Gas flow and the reactive shock for reacting gas flow), by splitting the phase volumes and rearranging them in space. This is actually an idea of redistribution of volume, mass, momentum and energy at the numerically

diffused interface region, by respecting the global conservation condition. Since this step does not involve the time evolution and that the genuinely nonlinear waves have been taken into consideration within the previous step by upwind strategy, the stability of the first-order DEM/RDEM method with piecewise constant volume fraction data is thus recovered using UDCS.

Let us also mention the UDCS limited second-order method has already been combined with the explicit two-step Runge-Kutta scheme (Predictor-Corrector scheme) for time discretization (see the combustion test case in Section 3.3). This allows to work with large enough CFL numbers when using a limited second-order reconstruction on all primitive variables (achieving quasi second-order accuracy in space and time). Unfortunately, it was found more difficult to couple the anti-diffusive UDCS approach with the second-order Runge-Kutta scheme (in the multi-dimensional case), so that achieving second-order accuracy both in space and time for multi-dimensional problems still requires further investigation.

Finally, as observed on the final 2D combustion problem, it will also be necessary to improve the approach used to compute the normal at the flame interface so as to avoid that the computation of this normal spoils the accuracy improvement brought by the anti-diffusive UDCS/RDEM. Note however that the second-order UDCS/RDEM approach, which represents a significant improvement of the classical second-order RDEM approach in terms of robustness, is now implemented in the fast dynamic fluid-structure interaction code EUROPLEXUS [12] to compute reacting flows in 3D large geometries [32, 38, 14] (*e.g.* the containment of the European Pressurized Reactor (EPR) [13]).

Acknowledgements

Appendix A. Non-conservative flux term treatment and summary of numerical fluxes for multi-D DEM/RDEM

Appendix A.1. Discretization of the non-conservative flux term

The following Baer-Nunziato type multiphase flow model for phase Σ_k is considered in this work:

$$\frac{\partial \left(\alpha_k \mathbf{U}_k\right)}{\partial t} + \nabla \cdot \left(\alpha_k \mathbf{F}_k\right) = \left(\mathbf{F}_{k,I} - \mathbf{U}_{k,I}\mathbf{D}_I\right) \cdot \nabla \alpha_k. \tag{A.1}$$

The (Reactive) Discrete Equations Method belongs to the Finite Volume family. Hence, the numerical discretization of the conservative flux term

$$\nabla \cdot \left(\alpha_k \mathbf{F}_k\right)$$

remains similar to what is done for classical conservation laws. The more delicate part is to deal with the non-conservative flux term

$$\left(\mathbf{F}_{k,I} - \mathbf{U}_{k,I}\mathbf{D}_I\right) \cdot \nabla \alpha_k. \tag{A.2}$$

Note that 1D local Riemann problems for Euler equations are solved in this paper to evaluate the numerical fluxes for multi-D problems. Let us consider one inlet cell boundary $\partial \mathcal{C}_{i,\text{in},j}$ (see Fig. 2) of an unstructured grid for the sake of demonstration. Note the case of an outlet cell boundary is treated in the same way. Fig. 2 is reproduced in Fig. A.1 and completed with flux computation details which are now reviewed. Three local 1D Riemann problems for Euler equations need to be solved (see also [35]). Here, we write

$$\left(\Sigma_k | \Sigma_{k'}\right)$$

to represent the 1D local Riemann problem for Euler equations between phase Σ_k and $\Sigma_{k'}$.

Let us project the non-conservative flux term (A.2) onto the normal direction $\vec{n}$ (pointing toward the inside of $\mathcal{C}_i$) of cell boundary $\partial \mathcal{C}_{i,\text{in},j}$, and write it as

$$\left(F_{k,I} - U_{k,I}D_I\right)\frac{\partial \alpha_k}{\partial \vec{n}}, \tag{A.3}$$
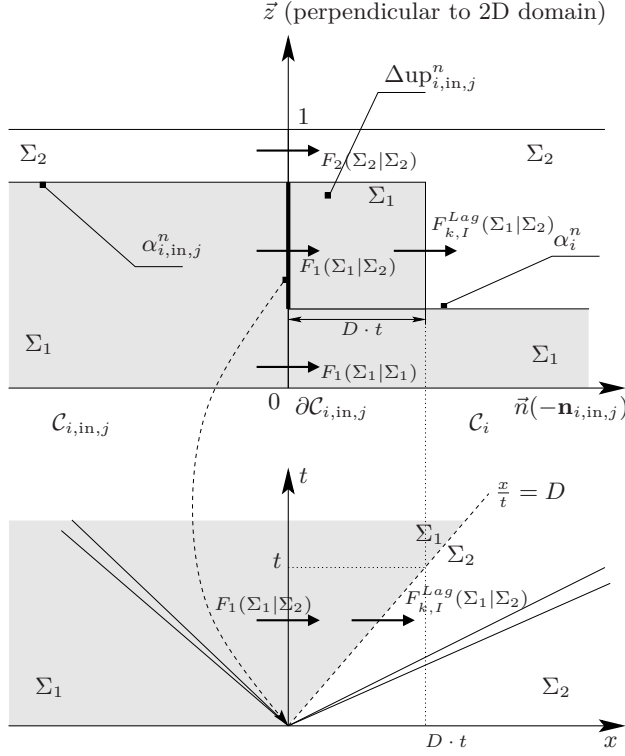
Figure A.1: Multi-D (Reactive) Discrete Equations Method (DEM/RDEM) on unstructured grids. $\vec{z}$ direction is perpendicular to the considered 2D domain. α is measured along $\vec{z}$. We consider the cell $\mathcal{C}_i$ and one of its inlet boundaries $\partial \mathcal{C}_{i,\text{in},j}$. Two single-phase and one two-phase (reactive) local Riemann problems for Euler equations require to be resolved. Grey represents phase Σ_1, and white is phase Σ_2. The numerical interface enters inside $\mathcal{C}_i$, which generates a positive volume $\Delta \text{up}_{i,\text{in},j}^n$ of Σ_1. The Eulerian Fluxes $F_1(\Sigma_1|\Sigma_1)$ and $F_2(\Sigma_2|\Sigma_2)$ are related to single-phase Riemann problems for Euler equations. The Eulerian Flux $F_1(\Sigma_1|\Sigma_2)$ and the Lagrangian Flux $F_{k,I}^{Lag}(\Sigma_1|\Sigma_2)$ are related to the two-phase Riemann problem for (reactive) Euler equations. All of these four fluxes at the considered cell boundary should be taken into account to update the phase space averages. On the top is the representation of an inlet cell boundary at the diffused interface region; on the bottom is the two-phase Riemann problem solution for (reactive) Euler equations on the $t-x$ plane.

with

$$
U = \begin{bmatrix} 1 \\ \rho \\ \rho v_{\vec{n}} \\ \rho \tilde{e}_t \end{bmatrix}, F = \begin{bmatrix} 0 \\ \rho v_{\vec{n}} \\ \rho v_{\vec{n}}^2 + p \\ \rho \tilde{e}_t v_{\vec{n}} + p v_{\vec{n}} \end{bmatrix},
$$

and

$$
v_{\vec{n}} = \mathbf{v} \cdot \vec{n},
$$

$$
D = \mathbf{D}_I \cdot \vec{n}.
$$

From a Finite Volume viewpoint at the discrete level, with first-order piecewise constant values of α, at the cell boundary $\partial \mathcal{C}_{i,\text{in},j}$, it can be observed that (A.3) only needs to be integrated at the discontinuity of α. Noticing that this discontinuity of α moves into $\mathcal{C}_i$ with a velocity D, the following integration can be carried out for (A.3) across this discontinuity within a time step Δt:

$$
\int_0^{\Delta t} \left(\int_{D \cdot t - \epsilon}^{D \cdot t + \epsilon} \left((F_{k,I} - U_{k,I} D) \frac{\partial \alpha_k}{\partial \vec{n}} \right) d\vec{n} \right) dt, \quad \text{(A.4)}
$$

with $\epsilon \to 0^+$. Note the Rankine–Hugoniot jump relation across the moving discontinuity yields

$$
F_{1,I} - F_{2,I} = (U_{1,I} - U_{2,I})D.
$$

Hence the so-called *Lagrangian Flux*

$$
F_{k,I}^{Lag} := F_{k,I} - U_{k,I} D \quad \text{(A.5)}
$$

is constant for the space integral in (A.4). Note moreover the local two-phase Riemann problem for Euler equations provides a self-similar solution. Thus, the integral (A.4) can be developed into:

$$
(F_{k,I} - U_{k,I} D) \cdot (\alpha_i^n - \alpha_{i,\text{in},j}^n) \Delta t. \quad \text{(A.6)}
$$

The Lagrangian Flux (A.5) is evaluated on the line

$$
\frac{x}{t} = D
$$

over the $t - x$ plane for Riemann problem solution.

Finally, the Finite Volume discretization (A.6) for the non-conservative flux term (A.3), together with the one for the conservation flux term, is used to update the space averages

$$
\alpha_k \mathbf{U}_k
$$

in the two-phase system of equations (A.1).

Note that, after also taking into account the total interfacial surface area $|\partial \mathcal{C}_{i,\text{in},j}|$, the first equation in (A.6) corresponds to the inlet generated volume (8) which reads:

$$
\Delta \text{up}_{i,\text{in},j}^n = \left(\alpha_{i,\text{in},j}^n - \alpha_i^n \right) |\partial \mathcal{C}_{i,\text{in},j}| D \Delta t,
$$

for the first-order discretization of topological equation with DEM/RDEM (see the formulation (7)).

32

The numerical fluxes of conservative and non-conservative terms (i.e. Eulerian and Lagrangian Fluxes, respectively) used in the DEM/RDEM approach, together with their corresponding partitioned area of volume fraction, are summarized as follows for cell boundary $\partial \mathcal{C}_{i,\text{in},j}$ in the normal direction $\vec{n}$ on Fig. A.1:

a) Phase Σ_1 in cell $\mathcal{C}_i$:

$$F_1(\Sigma_1|\Sigma_1) \cdot \alpha_i^n$$

$$F_1(\Sigma_1|\Sigma_2) \cdot (\alpha_{i,\text{in},j}^n - \alpha_i^n)$$

$$F_{1,I}^{Lag}(\Sigma_1|\Sigma_2) \cdot (\alpha_{i,\text{in},j}^n - \alpha_i^n)$$

b) Phase Σ_1 in cell $\mathcal{C}_{i,\text{in},j}$:

$$F_1(\Sigma_1|\Sigma_1) \cdot \alpha_i^n$$

$$F_1(\Sigma_1|\Sigma_2) \cdot (\alpha_{i,\text{in},j}^n - \alpha_i^n)$$

c) Phase Σ_2 in cell $\mathcal{C}_i$:

$$F_2(\Sigma_2|\Sigma_2) \cdot (1 - \alpha_{i,\text{in},j}^n)$$

$$F_{2,I}^{Lag}(\Sigma_1|\Sigma_2) \cdot (\alpha_{i,\text{in},j}^n - \alpha_i^n)$$

d) Phase Σ_2 in cell $\mathcal{C}_{i,\text{in},j}$:

$$F_2(\Sigma_2|\Sigma_2) \cdot (1 - \alpha_{i,\text{in},j}^n)$$

Appendix B. Limited variables reconstruction on unstructured grids

The space-reconstruction scheme used in this work is based on the *k*-exact reconstruction method applied to linear polynomial ($k = 1$) [9]. The generic variable q is assumed to be piecewise linear, i.e. in the generic i-th cell of the grid

$$q(\vec{r}) = q_i + \xi_i < \vec{\nabla}q >_i \cdot (\vec{r} - \vec{r}_i)$$

where q_i is the average value of the variable, $< \vec{\nabla}q >_i$ is the numerical gradient and ξ_i the limiter of the gradient.

Let us describe the evaluation of the numerical gradient. As displayed in Fig. B.2, a control volume (the stencil domain W) is defined for each cell, , which joins the centers of every adjacent cell. To
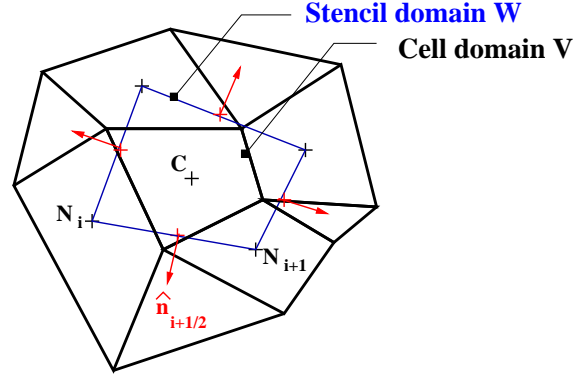

Figure B.2: Stencil for the numerical gradient evaluation. The element on the right is on the border: in this case it is assumed that $q(N_{i+1}) = q(C)$.

compute the numerical gradient of a generic variable q, $< \vec{\nabla}q >$, the Green-Gauss Theorem is applied to the stencil domain by considering a trapezoidal rule along each face of the element:

$$\int_W \vec{\nabla}q \, dV = \oint_{\partial W} q\hat{n} \, dS \ \Rightarrow$$

$$< \vec{\nabla}q > = \frac{1}{W} \sum_{\text{stencil}} \frac{q_i + q_{i+1}}{2} \hat{n}_{i+1/2} |N_i N_{i+1}|$$

where $q_i = q(N_i)$ and $|N_i N_{i+1}|$ is the length of the face $N_i N_{i+1}$.

As already mentioned, the following gradient reconstruction is linearly exact on both structured and unstructured meshes. Once the numerical gradient for the generic variable q is computed, it remains to evaluate the limiter ξ. Let us consider Fig. B.3. The evaluation of ξ is subjected to the condition that the reconstructed variables at each face, i.e.

$$q_{\text{left}} = q_i + \xi_i \, \vec{r}_{i,\text{Fk}} \cdot < \vec{\nabla}q >_i,$$

$$q_{\text{right}} = q_j + \xi_j \, \vec{r}_{j,\text{Fk}} \cdot < \vec{\nabla}q >_j$$

have to satisfy some properties. In 1D, if the "minmod" limiter is considered, the following property is satisfied:

$$q_i \leq q_j \Rightarrow q_{\text{left}} \leq q_{\text{right}}, \tag{B.1}$$

which allows the preservation of monotonicity of the solution of a convex scalar problem. Actually, in multi-dimensional domains, the same approach cannot be followed; the reason is obvious in regions of smooth flow. For example, let us compute a 1D
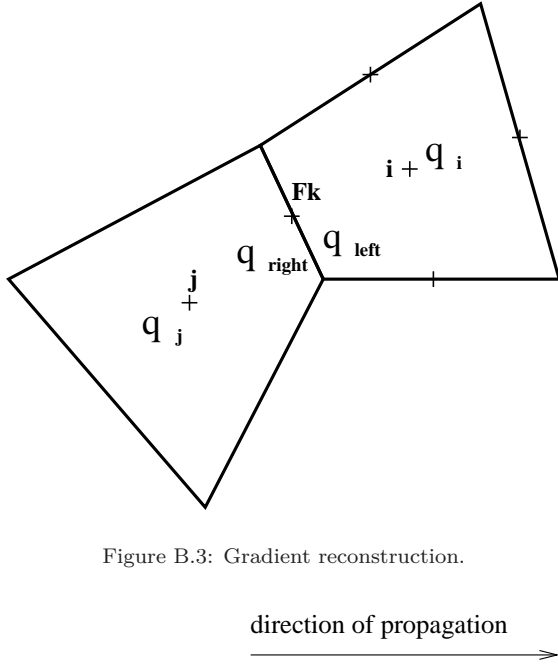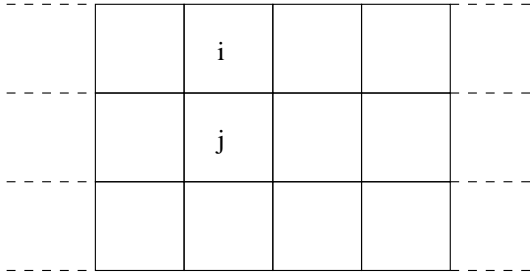
Figure B.3: Gradient reconstruction.

direction of propagation

Figure B.4: Computation of a physical 1D phenomenon in 2D mesh.

trema. A limiter satisfying this property is the Barth-Jespersen limiter (see [8]):

$$\xi_i = \min_{k \,\in\, \text{faces of } i\text{-th cell}} \xi_{i,k}, \qquad (B.2)$$

where

$$\xi_{i,k} =$$

$$\begin{cases} 1, & |\delta q| \le \epsilon(q_{\max} - q_{\min}); \\[2mm] \min\left\{1, \dfrac{q_{\max} - q_i}{\delta q}\right\}, & \delta q > \epsilon(q_{\max} - q_{\min}); \\[2mm] \min\left\{1, \dfrac{q_{\min} - q_i}{\delta q}\right\}, & \delta q \le -\epsilon(q_{\max} - q_{\min}); \end{cases}$$

$$\delta q = <\vec{\nabla} q>_i \cdot \vec{r}_{i,Fk},$$

$$q_{\max} = \max_{\text{stencil} \,+\, i} \{q_j\},$$

$$q_{\min} = \min_{\text{stencil} \,+\, i} \{q_j\},$$

physical problem in a multi-dimensional domain. In Fig. B.4 states in the i-th cell and in the j-th cell are physically the same but numerically different because of round-off errors. The projection of the numerical gradient onto the y direction is different from zero because of round-off errors; thus, even if the difference between the reconstructed values on the face between i and j depends only on round-off errors, the satisfaction of property (B.1)) may create unnecessary restrictions on the limited gradient in the i-th and j-th cells.

As already mentioned, another important property of scalar hyperbolic problems is the so-called LED (Local Extremum Diminishing) property: local extrema are bounded by their initial values. Thus, the variable reconstruction cannot create new ex-

with $\epsilon = 10^{-6}$, which prevents the smooth variation of the variable over a direction from creating an excessive restriction on the limiter (as in the case presented in Fig. B.4).

In this manner, at each face, the reconstructed value satisfies the condition $q_{\text{left}}, q_{\text{right}} \in [q_{\min}, q_{\max}]$.

Actually, the final target in the present work is the computation of flows which involve strong shock waves; thus, in order to enforce the stability, the property (B.1) should be at least satisfied on the faces relative to strong variations of q. Thus, let us suppose that for the cell i $q_{\max,i} = q_j$ and for the cell j $q_{\min,j} = q_i$. In that case, it can be shown that

34

$q_{\text{left}} > q_{\text{right}}$ if the limiter is computed as

$$
\xi_{i,k} =
\begin{cases}
1, & |\delta q| \leq \epsilon(q_{\max} - q_{\min}); \\[2em]
\min\left\{ 1, \dfrac{|\vec{r}_{i,\text{Fk}}|}{|\vec{r}_{i,\text{Fk}}| + |\vec{r}_{j,\text{Fk}}|} \dfrac{q_{\max} - q_i}{\delta q} \right\}, \\
& \delta q > \epsilon(q_{\max} - q_{\min}); \\[2em]
\min\left\{ 1, \dfrac{|\vec{r}_{i,\text{Fk}}|}{|\vec{r}_{i,\text{Fk}}| + |\vec{r}_{j,\text{Fk}}|} \dfrac{q_{\min} - q_i}{\delta q} \right\}, \\
& \delta q < -\epsilon(q_{\max} - q_{\min});
\end{cases}
\tag{B.3}
$$

with $\epsilon = 10^{-6}$.

References

[1] R. Abgrall and R. Saurel. Discrete equations for physical and numerical compressible multiphase mixtures. *Journal of Computational Physics*, 186:361–396, 2003.

[2] M. Baer and J. Nunziato. A two-phase mixture theory for the deflagration-to-detonation transition (ddt) in reactive granular materials. *International Journal of Multiphase Flow*, 12(6):861–889, November 1986.

[3] J.W. Banks, D.W. Schwendeman, A.K. Kapila, and W.D. Henshaw. A high-resolution Godunov method for compressible multi-material flow on overlapping grids. *Journal of Computational Physics*, 223(1):262–297, April 2007.

[4] A. Beccantini and E. Studer. The reactive Riemann problem for thermally perfect gases at all combustion regimes. *International Journal for Numerical Methods in Fluids*, 64:269–313, 2010.

[5] R. Borghi and M. Destriau. *La combustion et les flammes*. Editions Technip, 1995.

[6] A. Chertock, S. Karni, and A. Kurganov. Interface tracking method for compressible multifluids. *ESAIM : Mathematical Modelling and Numerical Analysis*, 42:991–1019, 2008.

[7] A. Chinnayya, E. Daniel, and R. Saurel. Modelling detonation waves in heterogeneous energetic materials. *Journal of Computational Physics*, 196(2):490–538, May 2004.

[8] M. Delanaye. *Polynomial Reconstruction Finite Volume Schemes for the Compressible Euler and Navier-Stokes Equations on Unstructured Adaptive Grids*. PhD thesis, Université de Liège, 1998.

[9] M. Delanaye and J.A. Essers. An accurate finite volume scheme for Euler and Navier-Stokes equations on unstructured adaptive grids. In *12th Computational Fluid Dynamics Conference (AIAA CFD Conf.)*, San Diego, June 1995. American Institute of Aeronautics and Astronautics.

[10] B. Després, F. Lagoutière, E. Labourasse, and I. Marmajou. An Antidissipative Transport Scheme on Unstructured Meshes for Multicomponent Flows. *The International Journal on Finite Volumes*, 7:30–65, 2010.

[11] D. A. Drew and S. L. Passman. *Theory of Multicomponent Fluids, Applied Mathematical Sciences, Vol. 135*. Springer, New York, 1998.

[12] EUROPLEXUS. A computer program for the finite element simulation of fluid-structure systems under transient dynamic loading. 28 May 2014. http://www-epx.cea.fr.

[13] EUROPLEXUS. Numerical simulation of hydrogen explosion in a reactor with Europleuxs. 28 May 2014. http://www-epx.cea.fr/index.php/what-is-epx/27-videos#Explo_H2.

[14] V. Faucher, P. Galon, A. Beccantini, F. Crouzet, F. Debaud, and T. Gautier. Hybrid parallel strategy for the simulation of fast transient accidental situations at reactor scale. In *SNA & MC 2013 - Joint International Conference on Supercomputing in Nuclear Applications + Monte Carlo, October 27-31, 2013*, La Cité des Sciences et de l'Industrie, Paris, France.

[15] V. Faucher and S. Kokh. Extended Vofire algorithm for fast transient fluid-structure dynamics with liquid-gas flows and interfaces. *Journal of Fluids and Structures*, 39:102–125, May 2013.

[16] E. Franquet and V. Perrier. Runge-Kutta discontinuous Galerkin method for interface flows with a maximum preserving limiter. *Computers & Fluids*, 65:2–7, July 2012.

[17] E. Franquet and V. Perrier. Runge-Kutta discontinuous Galerkin method for the approximation of Baer and Nunziato type multiphase models. *Journal of Computational Physics*, 231(11):4096–4141, June 2012.

[18] E. Franquet and V. Perrier. Runge-Kutta discontinuous Galerkin method for reactive multiphase flows. *Computers & Fluids*, 83:157–163, August 2013.

[19] J.-F. Haas and B. Sturtevant. Interaction of weak shock waves with cylindrical and spherical gas inhomogeneities. *Journal of Fluid Mechanics*, 181:41–76, 1987.

[20] M. Ishii and T. Hibiki. *Thermo-Fluid Dynamics of Two-Phase Flow*. Springer, New York, NY, second edition, 2011.

[21] A. Jameson. A perspective on computational algorithms for aerodynamic analysis and design. *Progress in Aerospace Sciences*, 37:197–243, 2001.

[22] S. Kokh and F. Lagoutière. An anti-diffusive numerical scheme for the simulation of interfaces between compressible fluids by means of a five-equation model. *Journal of Computational Physics*, 229(8):2773–2809, April 2010.

[23] J. J. Kreeft and B. Koren. A new formulation of Kapila's five-equation model for compressible two-fluid flow, and its numerical treatment. *Journal of Computational Physics*, 229(18):6220–6242, September 2010.

[24] A. L. Kuhl, M. M. Kamel, and A. K. Oppenheim. Pressure waves generated by steady flames. *Symposium (International) on Combustion*, 14(1):1201–1215, 1973.

[25] O. Le Métayer, J. Massoni, and R. Saurel. Modelling evaporation fronts with reactive Riemann solvers. *Journal of Computational Physics*, 205:567–610, 2005.

[26] T. Nonomura, K. Kitamura, and K. Fujii. A simple interface sharpening technique with a hyperbolic tangent function applied to compressible two-fluid modeling. *Journal of Computational Physics*, 258:95–117, February 2014.

[27] R.R. Nourgaliev, T.N. Dinh, and T.G. Theofanous. Adaptive characteristics-based matching for compress-

ible multifluid dynamics. *Journal of Computational Physics*, 213(2):500–529, April 2006.

[28] J. J. Quirk and S. Karni. On the dynamics of a shock-bubble interaction. *Journal of Fluid Mechanics*, 318:129–163, 1996.

[29] R. Saurel and R. Abgrall. A multiphase Godunov method for compressible multifluid and multiphase flows. *Journal of Computational Physics*, 150:425–467, 1999.

[30] R. Saurel and R. Abgrall. A Simple Method for Compressible Multifluid Flows. *SIAM Journal on Scientific Computing*, 21(3):1115, 1999.

[31] K.-M. Shyue. A wave-propagation based volume tracking method for compressible multicomponent flow in two space dimensions. *Journal of Computational Physics*, 215:219–244, 2006.

[32] E. Studer, A. Beccantini, S. Kudriakov, and A. Velikorodny. Hydrogen combustion modelling in large scale geometries. In *ICONE 21 - International Conference On Nuclear Engineering, July 29 - August 2, 2013*, Chengdu, China.

[33] K. Tang. *Combining Discrete Equations Method and Upwind Downwind-Controlled Splitting for Non-Reacting and Reacting Two-Fluid Computations*. PhD thesis, Grenoble Institute of Technology, 2012.

[34] K. Tang, A. Beccantini, and C. Corre. Combining Discrete Equations Method and upwind downwind-controlled splitting for non-reacting and reacting two-fluid computations. In *Seventh International Conference on Computational Fluid Dynamics (ICCFD7), Big Island, Hawaii, July 9-13*, 2012.

[35] K. Tang, A. Beccantini, and C. Corre. Combining Discrete Equations Method and upwind downwind-controlled splitting for non-reacting and reacting two-fluid computations: One dimensional case. *Computers & Fluids*, 93:74–90, April 2014.

[36] S. A. Tokareva and E. F. Toro. HLLC-type Riemann solver for the Baer-Nunziato equations of compressible two-phase flow. *Journal of Computational Physics*, 229(10):3573–3604, May 2010.

[37] M. A. Ullah, W. Gao, and D.-K. Mao. Towards front-tracking based on conservation in two space dimensions III, tracking interfaces. *Journal of Computational Physics*, 242:268–303, June 2013.

[38] A. Velikorodny, E. Studer, S. Kudriakov, and A. Beccantini. Combustion modeling in large scale volumes. In *ICHS 2013 - International Conference on Hydrogen Safety, September 9-11, 2013*, Brussels - Belgium.

[39] A. Zein, M. Hantke, and G. Warnecke. Modeling phase transition for compressible two-phase flows applied to metastable liquids. *Journal of Computational Physics*, 229(8):2964–2998, April 2010.